www.mycoordinates.org

Coordinates

Volume XVIII, Issue 5, May 2022

THE MONTHLY MAGAZINE ON POSITIONING, NAVIGATION AND BEYOND

Local Moho estimation using gravity inversion

Evaluation of KSACORS-based network GNSS-INS integrated system

In Coordinates

10 years before...

mycoordinates.org/vol-8-issue-5-May-2012

Crustal movement before and after the Great East Japan Earthquake

Dr Shunji Murai
Professor Emeritus, University of Tokyo, Japan
President, Japan Association of Surveyors,
Honorary Member of ISPRS and AARS

Dr Harumi Araki
Head, Research Laboratory of
Environmental Geology, Tokyo, Japan
Honorary Member of JSPRS

This paper summarizes the pre-signals before the earthquake which may be important information for predicting the occurrence of earthquakes as well as the crustal movement after the earthquake

Assisting visually impaired using smart-phone sensors

Oluropo Ogundipe
Research Fellow Nottingham Geospatial Institute, University of Nottingham, UK

A project at the University of Nottingham, is working to investigate indoor positioning and object recognition to aid the blind. As part of that project, tests were conducted to assess the quality of the various sensors of a smart-phone, the aim was to assess whether the smart-phone could be used as the sensor platform to enable the development of assistive technology for the visually-impaired.

The importance of mitigation of GNSS vulnerabilities and risks

Renato Filjar
FRIN MIET Research Engineer, Ericsson Nikola Tesla,
Zagreb, Croatia External Associate Professor, Faculty
of Maritime Studies, University of Rijeka, Croatia

Darko Huljeni
Ericsson Nikola Tesla, Zagreb, Croatia External
Assistant Professor, Faculty of Electrical Engineering
and Computing, University of Zagreb, Croatia

While a number of technology-related mitigation actions have already been deployed and then new and enhanced ones are under development, building the GNSS resilience should be extended to the user segment. National authorities should accept the responsibility for deployment of essential protective and mitigation activities addressing the GNSS-based systems and services of national importance.

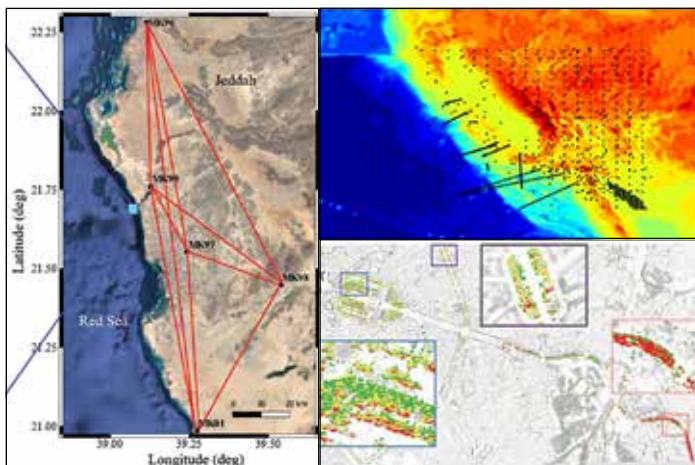## LAPSI: An EU thematic network for enabling public sector information re-use

Cristiana Sappa
Project Manager, LAPSI and EVPSI, Postdoctoral Researcher, Torino Law
School, Research Fellow, Nexa Center for Internet and Society, Italy

Giuseppe Futia
Communications Manager, NEXA Center for Internet &
Society, Politecnico di Torino – DAUIN, Italy

Clearly lots of work still needs to be done in the eld of PSI. Many legal aspects remain unclear and lots of doubts are there as to the technical issues, with particular reference to interoperability.

In this issue

Coordinates Volume 18, Issue 5, May 2022

Articles

Columns

Sagittarius A*

The recently released image

Captured by Event NASA's Event Horizon Telescope (EHT)

Said to be the first visual evidence of the black hole.

This could be made possible due to the efforts of more than 300 researchers from 80 institutions around the world.

Though the black hole cannot be seen itself,

The view captures light bent by the powerful gravity of the black hole.

The black hole - named as the Sagittarius A* (Sgr A*),

Lies in the centre of Milky Way

26,000 light years away from Earth.

This is said to be another evidence in support of Einstein's General Relativity.

What a feat it was and it is!

Bal Krishna, Editor
bal@mycoordinates.org

Local Moho estimation using gravity inversion

Gravity inversion is a useful tool for determining Moho depths in regions without having adequate seismic information

Dr H M I Prasanna
Senior Lecturer,
Faculty of Geomatics,
Sabaragamuwa
University of Sri Lanka,
Belihuloya, Sri Lanka

Composite of the Earth's Crust and Moho Estimation

Generally, the Earth is comprised three main internal structures: crust, mantle and core. These structures have different densities and seated in different depths. The innermost part of the Earth is the core and has the highest density. The solid inner core, which mainly consists of iron with a small amount of nickel, is surrounded by a liquid outer core and together with this outer core creates Earth's magnetism (Lowrie, 2007). The outermost part, the crust, covers the mantle which is located in between the core and crust and divided as upper and lower parts. Although the composition of solid lower mantle is poorly known, it is supposed to consist of magnesium and oxides of iron (Lowrie, 2007) and covered by plastic upper mantle. The crust together with the top layer of mantle, which is partially malted and bounded by the asthenosphere, is called the lithosphere and can be divided into seven or eight large pieces (or plates): African, Antarctic, Eurasian, North American, South American, Pacific and Indo-Australian (Indian and

Australian), and dozens of smaller plates (http://en.wikipedia.org/wiki/Plate_tectonics). Even though the crust contains very less volume of the Earth (less than 1%), the discovery of crust's properties is extremely important from a geological point of view since it is the place where all our geological resources like natural gas, oil and minerals come from.

The boundary between the Earth's crust and mantle is termed the Mohorovičić discontinuity, usually called Moho. A Croatian seismologist, named Andrija Mohorovičić first discovered this boundary in 1909. He noticed that seismograms from shallow-focus earthquakes had two sets of P (Primary) and S (Secondary) waves: one follows the direct path near the surface and the other refracted by the high density medium. He distinguished these two velocity mediums as lower and higher density interior layers where seismic waves acquire higher velocity in higher density medium. The lower density medium is now commonly referred to as Earth's crust while the higher density medium below the crust is known as Earth's mantle. The density interface
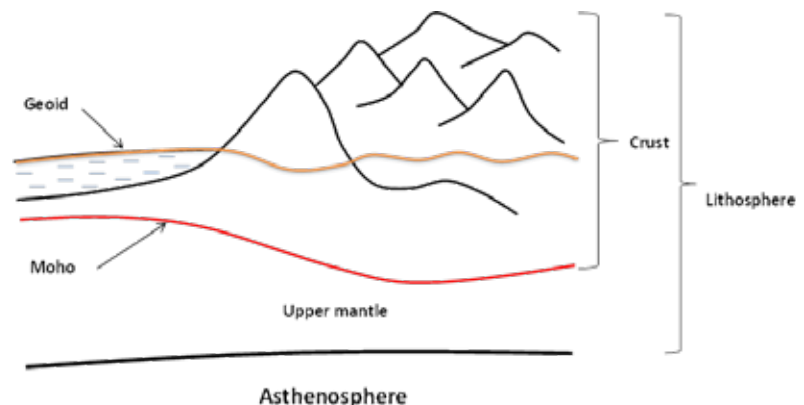

Figure 1: Definition of the Moho

between these two layers was named after him as Mohorovičić discontinuity (Moho). The realizing of Moho is vital from geological point of view because once the gravity effect of Moho structure is determined, it can be removed from observed gravity leaving the gravity effect of crustal structure which is important to identify the composite of the crust.

Moho estimation techniques

Generally, seismic and isostatic-gravimetric methods are used to determine Moho. The seismic methods usually provide a realistic way of imaging crust-mantle interface (Moho). However, the limited coverage of seismic data due to the cost and effort involved in collecting the data makes its application difficult for Moho estimation in some regions. An alternative could be the use of gravity data in isostatic-gravimetric methods. The main principle of isostatic methods which define topographic compensation masses is based on "equal-pressure and equal-mass" hypotheses. Two different methods have been developed at almost exactly the same time based on these hypotheses: Pratt-Hayforg system (1854) and Airy-Heiskanen system (1855). The former assumes varying crustal density with a uniform depth, termed as level of compensation. The latter supposes varying crustal thickness with uniform density, which forms roots and anti-roots. Both systems are highly idealized and assume the compensation to be local.

By introducing regional instead of local compensation, Vening Meinesz modified the Airy system in 1931 assuming that the crust is a homogeneous elastic plate floating on a viscous mantle (Bagherbandi and Sjöberg, 2012b) and later the system was further generalized and discussed by Moritz (1990) considering spherical effects. However, the homogeneity of plates is hardly believed since many geophysical evidences have proved that the density variations inside the plates and various non-isostatic effects introduce isostatic anomalies which violate the fundamental assumption of the inverse

problem of isostasy (Sjöberg, 2009). The isostatic-gravimetric methods of Moho estimation deal with this isostatic anomalies together with a suitable isostatic model and recently Vening Meinesz-Moritz isostatic model was used as it is the most realistic model among the traditional isostatic models. Isostatic anomalies can also be used as a classical-spectral approach of Moho estimation (Braitenberg et al., 2000).

The pure gravimetric method of Moho estimation is based on an inversion of the gravity data. Usually, Bouguer anomalies are used for the inversion. The advantage of gravity inversion is the accessibility of gravity data since the satellite gravity data together with the terrestrial data provides a sufficient coverage for the whole globe (Block et al., 2009). The global geopotential models are also an important source of gravity information (Reguzzoni and Sampietro, 2012). The most important role of gravity inversion method is to extract the appropriate anomalies related to Moho deflection. Many techniques have been employed to isolate anomalies associated with these Moho discontinuities (Lefort and Agarwal, 2000). Spectral methods are used to filter short and long wavelength effects of gravity stem from intracrustal/superficial inhomogeneities and deep seated sources (Sjoberg, 2009). To decide which wavelengths should be filtered out or which range of wavelengths should be used is very difficult and complex. It usually depends on the target depth, spectrum analysis of the gravity anomaly, and other geophysical or geological information (Gomez-Ortiz et al., 2011).

The global Moho models

Seismic methods of Moho estimation are based on the changes of the velocity of the propagated seismic waves between the crust and mantle. CRUST5.1 is the first official global seismic crustal model published by Mooney et al. (1998). The resolution of this model is 5° x 5°. This model is updated to CRUST2.0 by Bassin et al. 2000 (resolution 2° x 2°) employing the seismic data published in the period

1984-1995. Now CRUST1.0 model is available with 1° x 1° resolution (https://igppweb.ucsd.edu/~gabi/crust1.html). This model gives rather comprehensive density structure of the crust and upper mantle. The model comprises seven layers: ice, water, soft sediments, hard sediments, upper crust, middle crust and lower crust. The 7th layer (lower crust) represents the Moho depths with respect to MSL. Apart from the elevations of the different density layers, the model gives the density variation of each layer.

The first global high resolution (0.5° x 0.5°) map of Moho depths, GEMMA (GOCE Exploitation for Moho Modeling and Applications), was compiled based on data from ESA's GOCE gravity satellite. This global model is computed by inverting the global grid of second radial derivative of the gravitational potential (gravity gradient) observed by GOCE satellite and considering the density of the crust as defined in the CRUST2.0 model. For the computation of this model, gridded satellite data have been combined with sparse ground data using collocation (Reguzzoni and Sampietro, 2012). GEMMA global and local models are available at http://geomatica.como. polimi.it/elab/gemma/.

Even though global Moho models cover whole globe, their accuracies are not well specified. The accuracy of global seismic CRUST models depends on the data availability and is varies from place to place. For instance, the model gives more accurate Moho depths in United States and Europe since most of the seismological data are confined to these regions (see the distribution of global seismological data and network stations at http://www.isc.ac.uk/ and http://www.iris.edu/hq/programs/gsn). The accuracy of GEMMA model is also not consistent in continental and marine regions due to the variation of crust-mantle density contrast.

Gravity inversion

One of the fundamental challenges of geophysical study is to determine the

geometry of subsurface structure (density interfaces) from gravity anomaly. One such an important application is to map crust-mantle boundary (Moho) from surface gravity anomaly. The solution of this problem can be categorized into two main modeling techniques: forward and inverse (Ebbing et al., 2001). In forward modeling method, the gravity effect is computed for an initial model source body constructed based on geological and geophysical intuition and then compared with the observed gravity anomaly. The final source body is developed by adjusting model parameters to fit the computed and observed anomalies.

In the inverse method, the parameters of the perturbing body are computed directly from the observed anomalies. This method becomes more popular after adopting FFT algorithms. Braitenberg et al. (1997) proposed an iterative method from isostatic gravity anomalies with an initial isostatic Moho. The other important FFT application in gravity forward modeling was presented by Parker (1973). He expressed the total gravitational anomaly due to uneven, non-uniform layer of material in terms of its Fourier transform by means of the sum of Fourier transforms of powers of the surface affecting the anomaly. The corresponding inverse scheme was presented by Oldenburg (1974). He rearranged Parker's forward algorithm to determine the density interface from the observed gravity anomaly. Although the original form of Parker-Oldenburg's algorithms is two-dimensional (2D), its three-dimensional (3D) application with large data sets in geophysical field can still be frequently found now (Gómez–Ortiz and Agarwal, 2005). The Parker-Oldenburg algorithms were used in this article for numerical analysis.

Usually high frequency filtered Bouguer gravity anomaly data is used for Moho depth estimation from gravity inversion. As mentioned earlier, the extraction of the most relevant gravity anomaly that reflects main Moho deflections is complex since the harmonics of the short wavelength features could be mixed with that of long

wavelength features. To overcome this difficulty, various filtering techniques are used. Spectral methods are used to filter short and long wavelength effects of gravity that stem from intracrustal/superficial inhomogeneities and deep seated sources (Sjöberg, 2009). However, to decide which wavelengths should be filtered out or which range of wavelengths should be used is very difficult and complex. It usually depends on the target depth, spectrum analysis of the gravity anomaly, and other geophysical or geological information.

Gravity data filtering and spectral analysis

Usually, the shallow gravity effects are due to intracrustal and superficial inhomogeneities (Bagherbandi et al., 2013). Although spectral window method (Spector and Grant, 1970) removes short wavelength effects of gravity data, some shallow features such as the sedimentary cover are broadband. This demonstrates that the effects of these shallow features cannot be removed completely by spectral filtering (Corchete et al., 2010). Therefore, the gravity effect of sedimentary layer should be removed first from Bouguer anomalies before starting spectral analysis (Sjöberg, 2009), otherwise the spectrum of features at shallow depths could overlap spectrum of deep features (as Moho undulations).

To obtain the gravity anomalies associated with the lithosphere structure, the gravity effect of features deeper than lithosphere and non-isostatic effects must be subtracted. The main long wavelength gravity effects are coming from density variation of Earth's mantle and core/mantle structure variations (Martinec, 1994). These deep mass anomalies and other various long wavelength gravity effects can be categorized as non-isostatic effects which correspond to the influence of different geophysical mechanisms such as crustal thickening/thinning due to thermal expansion of mass of the mantle, mantle convection, plate movements and flexure (Watts,

2001). Generally, if the topography contains features longer than ~500 km, it may contain a component of the surface expression of mantle convection (Crosby, 2007). However, a proper analysis is needed since the depth of these source structures is location dependent. These deep gravity effects are estimated from the spectral depth of the gravity signal using the degree based on Bruns' formula (Bagherbandi and Sjöberg, 2012a).

Numerical study

Numerical studies were carried out in a test region of USA, bounded by latitudes 30–43 N and longitudes 128–112W, where reasonably accurate seismic Moho depths were available for validation of the results. The Parker-Oldenburg algorithms were used for the computations (Prasanna et al, 2012).

A dataset of 1193 seismic Moho depths, which were compiled from numerous seismic observations and datasets of this area (Tape et al., 2012), was used for comparison of the results. According to this data, the average Moho of this area is about 26 km with minimum 6 km and maximum 53 km. The large variation of the Moho is the result of the transition from oceanic crust to continental crust. The average uncertainty of this published Moho was 2.3 km.

The gravity effect of sedimentary layer was removed based on CRUST2.0 model. For long wavelength correction, it was assumed that the mean crustal thickness would be less than 40 km (According to CRUST2.0 and the seismic data, the mean Moho depth of the area is 23 km and 26 km respectively). Therefore, the spectral depth up to 40 km, were excluded, based on spectral depth estimation, as being caused by non-isostatic effects. The remaining Bouguer anomalies were used for spectral analysis to find the appropriate frequency range related to Moho deflection. From spectral analysis we found that the wavelength range 157–95 km was most accountable for mean CRUST2.0 Moho depth.
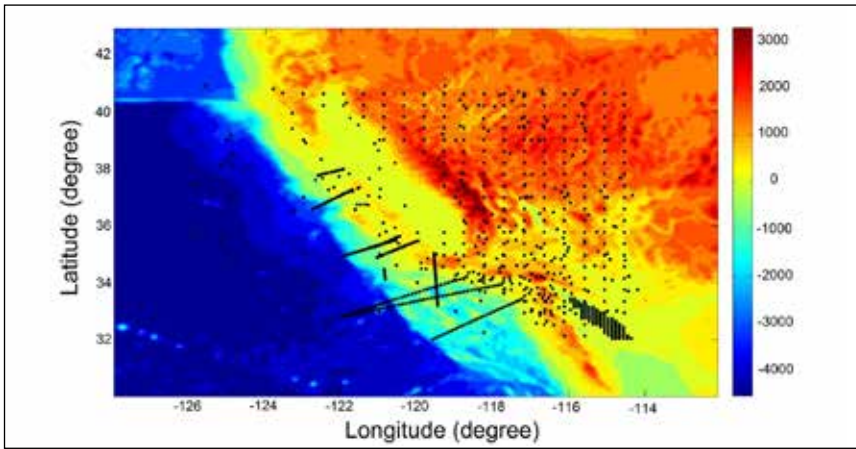
Figure 2: Topography/bathymetry variation of the area. Heights obtained from DTM2006.0. The locations of seismic points are marked. Values are given in meters.
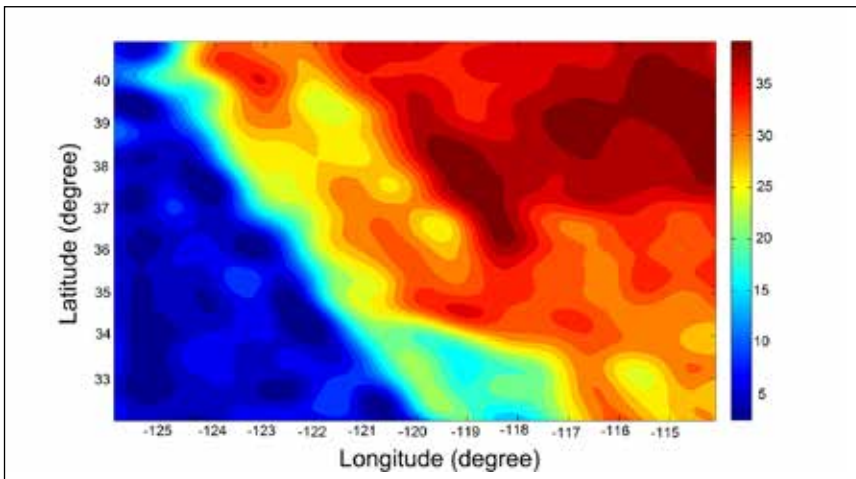

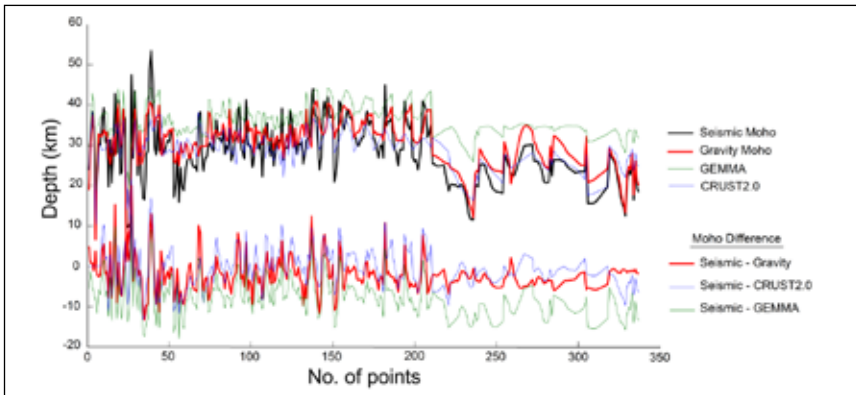**Figure 3: Moho depth variations of the test area. Values are given in km.**

Figure 4: The comparison of the computed gravity Moho with various Moho depths in the test area.

Table 1: The statistics of the difference between seismic and various Moho depths of the test area (Range = Min–Max).

	Seismic – Gravity Moho	Seismic – Crust2.0	Seismic – GEMMA
Range(km)	33.3	35.1	30.6
Mean (km)	-2.2	-0.6	-8.2
STD (km)	4.1	4.7	4.8

Finally, the high cut-off filter was used with the selected frequency range to determine the Moho surface (Figure 3) following the inversion process.

To validate the results of the test area, a part of the dataset (337 points) located well within the test area was selected from the available seismic database. Additional comparisons were made using CRUST2.0 and GEMMA global Moho depths. Figure 4 and Table 1 show the statistics of the comparison.

The comparison was carried out at three levels. First, the gravity Moho depths are compared with seismic Moho depths. This will give the actual deviation of the gravity Moho surface. Secondly, the difference with CRUST2.0 Moho will show how consistent the gravity Moho surface is with the best global seismic Moho model available so far. Finally, we will test our computed gravity Moho against a global gravity Moho model (GEMMA) compiled from different techniques.

Generally, our computed Moho depths are well-consistent with the seismic Moho depths (correlation coefficient is around 0.8). From Table 1, we could notice that all three different Moho depths have a similar standard deviation range (4–5 km standard deviation of the difference). However, the mean difference between our computed gravity Moho and the actual seismic Moho is significantly lower than that of GEMMA Moho. The possible reason of having a large bias in GEMMA Moho (8.2 km) would be that the density contrast of Moho interface used in GEMMA project is significantly different from the seismic Moho interface. The bias of our computed gravity Moho (2.2 km) could be due to using the mean value of density contrast (0.4 g/cm³). However, this bias may be acceptable since the average uncertainty of seismic Moho is 2.3 km (Tape et al., 2012). CRUST2.0 Moho is almost consistent with observed seismic Moho. This is expected, because the most of seismic points in this area are included in CRUST2.0 model. Finally, we could

say that our computed Moho obtained is more or less the same quality (our model is slightly better) as Global Moho models, and most importantly our Model is better in terms of the resolution (5 arc min).

Conclusion

Moho depths were computed using an interactive way of gravity inversion method constrained with seismic information (CRUST2.0 data). The result of the test area demonstrated that it has better consistency with seismic Moho depths than global Moho depths in terms of resolution and accuracy, suggesting that this method is suitable for high resolution local Moho depth determination, especially for areas without adequate seismic data.

The determination of Moho surface is important in various geophysical studies, such as studies of crustal and lithosphere signature and flexure studies. Usually, geophysical/structural studies deal with large areas, for instance, continental or regional studies. However, the recovery of local Moho with high resolution is important for local geophysical studies, such as studies of density distribution of the crust and small-scale subduction

References

Bagherbandi, M. and Sjöberg, L. E. (2012a). Non-isostatic effects on crustal thickness: A study using CRUST2.0 in Fennoscandia. Physics of the Earth and Planetary Interiors, 200-201, 37-44.

Bagherbandi, M. and Sjöberg, L. E. (2012b). A synthetic Earth gravity model based on a topographic-isostatic model. Studia Geophysica et Geodaetica, 56(4), 935-955.

Bagherbandi, M., Tenzer, R., Sjöberg, L. E. and Novák, P. (2013). Improved global crustal thickness modeling based on the VMM isostatic model and non-isostatic gravity correction. Journal of Geodynamics, 66, 25-37.

Bassin, C., Laske, G. and Masters, G. (2000), The current limits of resolution for surface wave tomography in North America, EOS Trans. AGU, 81(48), Fall Meet. Suppl., Abstract S12A-03.

Block, A. E., Bell, R. E. and Studinger, M. (2009). Antarctic crustal thickness from satellite gravity: Implications for the Transantarctic and Gamburtsev subglacial mountains. Earth and Planetary Science Letters, 288(1), 194-203.

Braitenberg, C., Pettenati, F. and Zadro, M. (1997). Spectral and classical methods in the evaluation of Moho undulations from gravity data: The NE Italian Alps and isostasy. Journal of Geodynamics, 23, 5-22.

Braitenberg, C., Zadro, M., Fang, J., Wang, Y. and Hsu, H. T. (2000). Gravity inversion in Qinghai-Tibet plateau. Phys. Chem. Earth, 25(4), 381-386.

Corchete, V., Chourak, M. and Khattach, D. (2010). A methodology for filtering and inversion of gravity data: An example of application to the determination of the Moho undulation in Morocco. Engineering, 2(3), 149-159.

Crosby, A. G. (2007). An assessment of the accuracy of admittance and coherence estimates using synthetic data. Geophysical Journal International, 171, 25-54.

Ebbing, J., Braitenberg, C. and Götze, H. J. (2001). Forward and inverse modelling of gravity revealing insight into crustal structures of the Eastern Alps. Tectonophysics, 337, 191-208.

Gómez-Ortiz, D. and Agarwal, B. N. P. (2005). 3DINVER.M: A MATLAB program to invert the gravity anomaly over a 3D horizontal density interface by parker-oldenburg's algorithm. Computers & Geosciences, 31, 513-520.

Gómez-Ortiz, D., Agarwal, B. N. P., Tejero, R. and Ruiz, J. (2011). Crustal structure from gravity signature in the Iberian Peninsula. Geological Society of America Bulletin, 123(7-8), 1247-1257.

Lefort, J. P. and Agarwal, B. N. P. (2000). Gravity and geomorphological evidence for a large crustal bulge cutting across Brittany (France): A tectonic response to the closure of the Bay of Biscay. Tectonophysics, 323(3–4), 149-162.

Lowrie, W. (2007). Fundamentals of geophysics (Second edition), Cambridge University Press.

Martinec, Z. Ě. K. (1994). The minimum depth of compensation of topographic masses. Geophysical Journal International, 117(2), 545-554.

Moritz, H. (1990). The Figure of the Earth. H Wichmann, Karlsruhe.

Oldenburg, D. W. (1974). The inversion and interpretation of gravity anomalies. Geophysics, 39(4), 526-536.

Parker, R. L. (1973). The rapid calculation of potential anomalies. Geophysical Journal of the Royal Astronomical Society, 31, 447-455.

Reguzzoni, M. and Sampietro, D. (2012). Moho estimation using GOCE data: A numerical simulation. In S. C. Kenyon, M. C. Pacino and U. J. Marti (Eds.), International Association of Geodesy symposia, "geodesy for planet earth", Springer, Verlag, Berlin, 205-214.

Sjöberg, L. E. (2009). Solving Vening Meinesz-Moritz inverse problem in isostasy. Geophysical Journal International, 179(3), 1527-1536.

Spector, A. and Grant, F. S. (1970). Statistical methods for interpreting aeromagnetic data. Geophysics, 35, 293-302.

Watts, A. B. (. (2001). Isostasy and flexure of the lithosphere. Cambridge University Press, Cambridge, New York, Melbourne.

Evaluation of KSACORS-based network GNSS-INS integrated system for Saudi coastal hydrographic surveys

This paper evaluated a real-time KSACORS-based NRTK GNSS-INS integrated solution and a post-processed KSACORS-based NPPK GNSS-INS integrated solution

Mohammed El-Diasty
PhD, P. Eng.
Civil and Architectural
Engineering Department,
College of Engineering,
Sultan Qaboos University,
Muscat, Oman

Abstract

Multibeam echosounding technique is used to provide sea-floor mapping with relatively high-quality level and requires an accurate positioning and attitude system. Integration of Global Navigation Satellite System (GNSS) and inertial navigation system (INS) is widely used for positioning and attitude control and is carried out using an inertial unit integrated with GNSS solution to provide the required accuracy. Recently, the Kingdom of Saudi Arabia Continuously Operating Reference Station (KSACORS) network GNSS stations were developed by the Saudi Geodetic Commission for Survey (GCS) to maintain an accurate GNSS positioning solution for governmental and private sectors within Saudi Arabia coverage area. This paper investigates the performance of the KSACORS-based network GNSS-INS integration for Saudi coastal hydrographic surveys and also investigates whether the archived accuracy fulfill International Hydrographic Organization (IHO) standards for all survey orders. To meet this objective, the KSACORS-based network real-time-kinematic (NRTK) and network post-processed kinematic (NPPK) solutions are integrated with INS solution. The implementa-tion of the KSACORS-based NRTK and NPPK GNSS-INS integration methods shows that centimeters and arc-minutes level of accura-cies for position

and attitude solutions, respectively, can be success-fully achieved throughout onshore hydrographic surveys. Also, it is shown that the KSACORS-based NRTK GNSS-INS and NPPK GNSS-INS integration systems fulfill IHO standards for all survey orders and can be employed for Saudi coastal multibeam echosounding surveys. The significant contribution of the paper is that it imple-mented the performance of KSACORS-based NRTK GNSS-INS and NPPK GNSS-INS integration systems for hydrographic surveying application and validated their accuracies against IHO standards.

1. Introduction

Over the past years, positioning at sea for hydrographic surveying, navigation, and other operations, has been revolutionized by the use of the Global Navigation Satellite System (GNSS). There are several modes in which GNSS can be used, yielding a progression of improving three-dimensional position accuracies (at the 95%confidence level) such as single receiver in autonomous mode (10-20 m accuracy), differential code in standard DGNSS mode (1-5 m accuracy), differential carrier-phase with floating-point cycle ambiguities (0.2-0.8 m accuracy), Precise Point Positioning (PPP) mode (0.1-0.2 m accuracy) and differential carrier-phase with fixed-

integer cycle ambiguities in Real-Time Kinematic (RTK) and Post-Processed Kinematic (PPK) modes (0.01-0.05 m accuracy) (Hofmann-Wellenhof et al. 2008; El-Diasty 2016). All these modes are in common use. Sub-decimeter marine vertical positioning accuracies are required for the measurement of water level variations (tides, etc.), hydrographic surveying, navigation and other marine operations. For modern hydrographic surveys, multibeam echosounding is widely employed to provide sea-floor mapping with relatively high-quality level and 100% coverage and is capable of delin-eating seabed features at the centimeters level in shallow water hydrographic surveys. Because of their wide-swath, an accurate positioning and attitude system is required to accurately geo-referencing the multibeam echosounder. Integration of GNSS and Inertial Navigation System (INS) is widely used for positioning and attitude of the hydrographic surveying vessel. Integration of GNSS and INS is carried out using an inertial unit integrated with RTK-based or PPK-based GNSS solution using GNSS receivers in the survey area along with a base GNSS receiver at accurately known coordinate to provide the required position and attitude accuracy recommended by the International Hydrographic Organization (IHO) (El-Diasty 2010). However, the requirement of setting up a base GNSS station in the survey area for RTK-based and PPK-based GNSS system increases the positioning system cost and hence the RTK-based and PPK-based GNSS-INS systems are considered as an expensive GNSS posi-tioning system. Moreover, with traditional single-base RTK-based and PPK-based GNSS processing, it is always necessary to be within 20 to 30 km of a base station sometime during the survey mission in order to resolve the ambiguities. If the distance is greater than 20 to 30 km from a reference station, the residual error caused by the atmosphere delaying the GNSS signals reaches a required reliable magnitude to fix carrier ambiguities and provide centimeters level of accuracy (Hutton et al. 2007, 2008). Advances in a Continuously Operating Reference Stations (CORS) network

technology at national and international levels have shown promising light towards the development of an autonomous and low cost GNSS solution for position-ing applications where one GNSS receiver (rover) is only employed. The typical dis-tances between CORS network stations are usually designed to span between 50 to 70 km and can transmit a Network-based Real-time Kinematic GNSS data of a Virtual Reference Station (NRTK_VRS) to a roving station in Radio Technical Commission for Maritime (RTCM) format from the CORS control centers to provide centimeters level of accuracy (Landau et al. 2002; Tusat 2018). Also, the archived GNSS observation data from the CORS network stations can be employed in Network-based Post-Process Kinematic mode to generate a virtual post-processed VRS station (NPPK_VRS) to provide centimeters level of accuracy (Hutton et al. 2007, 2008). Recently, the Saudi KSACORS network GNSS stations were developed by Saudi Geodetic Commission for Survey (GCS) to maintain an accurate GNSS positioning solution for governmental and private sectors within Saudi Arabia cover-age area. This paper investigates the performance of network GNSS-INS integration using a most recently lunched national KSACORS network GNSS corrections (offi-cially launched on April 2013) to obtain a precise position and attitude solution for Saudi coastal hydrographic surveys. This paper also investigates whether the archived accuracy fulfill the International Hydrographic Organization (IHO) standards for all hydrographic survey orders. The investigated real-time KSACORS-based NRTK GNSS-INS position and attitude solution can be considered as an alternative low-cost approach when compared with RTK-based GNSS-INS solution. Also, the investigated post-processed KSACORS-based NPPK GNSS-INS position and attitude solution can be considered as an alternative low-cost approach when compared with PPK-based GNSS-INS solution.

To examine the performance of the proposed KSACORS-based NRTK and NPPK GNSS-INS integrated system for

hydrographic surveys, kinematic GNSS and inertial data for two survey tests were collected onboard a hydrographic surveying vessel using Applanix position and orientation system for marine vessels (POS-MV). POS-MV is comprised of a dual frequency GNSS receiver (BD982 by Trimble) and tactical-grade inertial measurement unit (IMU) (LN-200 by Northrop Grumman). To meet the paper objective, the KSACORS-based NRTK and NPPK GNSS solution was integrated with INS to provide an accurate position and attitude solution for the hydrographic surveying vessel. Then, the accuracy of the proposed system was investigated whether it can meet the international standards (IHO standards) for hydrographic surveys performed by multibeam echosounder. In principle, the accuracy represents the difference between the proposed solutions (systems under investiga-tion) and the reference solution (considered as a "truth" solution) and it is investi-gated based on the estimated root-mean-square (RMS) errors. The main contribution of the paper lies in two folds. First, the paper implements the performance of KSACORS-based NRTK GNSS-INS and NPPK GNSS-INS integration systems for hydrographic surveying application. Second, the achieved accuracies from the two GNSS-INS integrated systems under investigation are validated against IHO stands for all hydrographic survey orders.

2. KSACORS–based NRTK and NPPK GNSS–INS navigation solution

Network CORS solution has proven that it is a valuable method for accurate position-ing which can be applied over a national scale. By the presence of the CORS network, the GNSS solution accuracy can reach centimeters level of accuracy (Ulrich et al. 2000; Retscher 2002; Wei et al. 2006; Hofmann-Wellenhof et al. 2008). Currently, the Saudi KSACORS network corrections provide an accurate GNSS corrections for net-work real-time kinematic (NRTK) and network post-processed kinematic (NPPK) applications. KSACORS

utilizes the GNSS data from about 200 continuously operat-ing GNSS stations, as shown in Figure 1, to estimate the network corrections (Golubinka 2018; GCS 2019). The KSACORS control center takes the responsibility to process the data from KSACORS stations and estimate the real-time GNSS errors (ionospheric error, tropospheric error, orbital error and carrier phase ambiguities fix) and generate a GNSS observation data of a Virtual Reference Station (VRS) in stand-ard RTCM format for real-time GNSS solution for the end user, however, the raw observation data of all KSACORS stations are stored in the KSACORS repository for post-processing solution. In real-time mode, the RTCM data are delivered to end user over the Network Transport of RTCM by Internet Protocol (NTRIP) by the KSACORS control center (Alomar et al. 2018) to achieve NRTK solution. The real-time RTCM data are classified to types of corrections, so called "NRTK_VRS" for applications that require centimeters level of accuracy and "DGNSS_VRS" for applica-tions that require decimeters to a meter level of accuracy. However, in the post-processing mode, the NPPK solution can be achieved using a post-processed virtual reference station (SmartBase) generated from multiple GNSS stations data down-loaded from the KSACORS website. Typically, three GNSS CORS stations can be employed to generate a SmartBase (VRS

station), however, a minimum of four GNSS CORS stations are recommended to provide a more robust GNSS positioning solution (Hofmann-Wellenhof et al. 2008; Hutton et al. 2008). The integration of KSACORS-based NRTK and NPPK GNSS positioning system with inertial navigation system are evaluated in this paper. The baselines for the CORS stations are usually designed to be within a range of 50-70 km to achieve centimeters level of accuracy (Retscher 2002; Rizos and Han 2003).

Figure 2 shows how the KSACORS control center receives the real-time raw GNSS data form all CORS network stations and process it to estimate the GNSS errors (ionospheric error, tropospheric error, orbital error and carrier phase ambiguities fix) based on static CORS network stations of accurately estimated coordinates that were employed to realize the Saudi national geodetic reference frame (Golubinka 2018). Then the KSACORS control center generates NRTK_VRS GNSS data in standard RTCM format (Alomar et al. 2018). The end user with GNSS rover can receive real-time RTCM corrections via NTRIP protocol using an internet access to KSACORS web for an authorized user. Moreover, the GNSS observation data for all stations are archived in KSACORS repository server for post-processed network-based GNSS solution. The real-time NRTK and post-processed NPPK GNSS positioning are com-mon in implementing VRS concept. The details of VRS observation generation algo-rithms can be found in Wei et al. (2006) and Hofmann-Wellenhof et al. (2008).

The GNSS data (pseudoranges and carrier phases) and inertial data (accelerometers and gyros measurements) of rover along with GNSS data of VRS base are integrated in a tightly coupled scheme to provide the KSACORS-based NRTK and NPPK GNSS-INS Navigation solution. The observations from GNSS VRS base and GNSS rover are integrated with INS navigation system in tightly coupled scheme using Klaman filter to estimate the high accurate navigation solution and associated uncer-tainties. The Kalman filter constructs double differences of these observations at the rover and VRS base. The Inertially Aided Double Differenced (IADD) pseudorange observable Z_P^{IADD} and phase observable Z_Φ^{IADD} for a single baseline between rover and VRS base are represented in the following forms (Scherzinger 2000):

$$Z_P^{IADD} = \nabla\Delta r(\hat{X}_{INS}, X_{VRS}) + \nabla\Delta P \tag{1}$$

$$Z_\Phi^{IADD} = \nabla\Delta r(\hat{X}_{INS}, X_{VRS}) + \nabla\Delta\Phi - \lambda\nabla\Delta N_0 \tag{2}$$

where, $\nabla\Delta r(\hat{x}_{INS}, x_{VRS})$ is the double differenced range, $\hat{x}_{INS}$ is the computed position vector from inertial navigation mechanization (inertial navigator), x_{VRS} is the VRS base position vector, $\nabla\Delta P$ is the double differenced pseudorange, $\nabla\Delta\Phi$ is the double differenced carrier phase (in meter) and N_0 is the initial integer ambiguity.

From all double differenced observables, the measurement model of the errors can be written in two compact forms as (Scherzinger 2002):
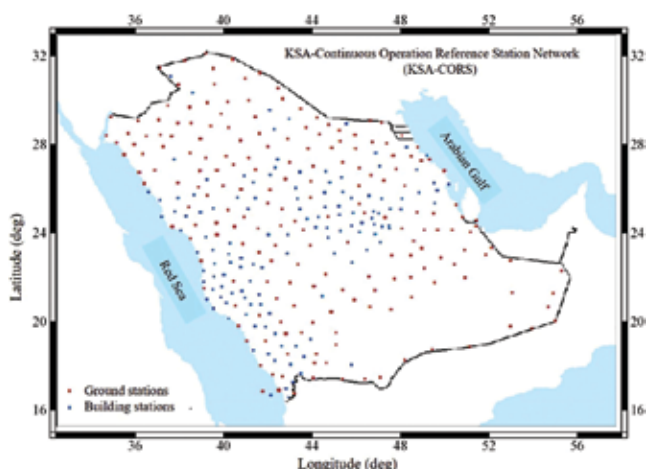

Figure 1. The KSACORS network of about 200 continuously operating GNSS stations (GCS. 2019).

Figure 2. The KSACORS Control Unit Structure.

$$\begin{bmatrix} Z_P^{IADD} \\ Z_\Phi^{IADD} \end{bmatrix} = \begin{bmatrix} BA & 0 & 0 \\ BA & 0 & \lambda I \end{bmatrix} \begin{bmatrix} x_n \\ x_s \\ x_a \end{bmatrix} + \begin{bmatrix} \varepsilon_P \\ \varepsilon_\Phi \end{bmatrix} \qquad (3)$$

$$Z_k^{IADD} = Hx + \varepsilon \qquad (4)$$

where, B is the double differenced matrix, A is the single differenced matrix, λ is the is the wavelength of the carrier phase chosen, ε_P is the model noise when pseaudorange observable is implemented, ε_Φ is the model noise when phase observables are implemented, x_n is the inertial navigator error state vector (3 inertial position errors, 3 inertial velocity errors), x_s is the inertial sensor error state vector (3 attitude errors, 3 gyros biases, 3 accelerometer biases), x_a is the aiding sensor error state vector comprised of the GNSS double differencing phase ambiguities state vector with size of n-1 where n is the number of phase observations, x is the full error state vector and H is the design matrix. To estimate the error state vector using Klaman filter implementation, the system model (state model) is required. The state model represents the system error model dynamics (see for more details). The generic structure of the con-tinuous-time state model takes the following form (Brown and Hwang 1997):

$$\frac{d}{dt} \begin{bmatrix} x_n \\ x_s \\ x_a \end{bmatrix} = \begin{bmatrix} F_n & F_{ns} & 0 \\ 0 & F_s & 0 \\ 0 & 0 & F_a \end{bmatrix} \begin{bmatrix} x_n \\ x_s \\ x_a \end{bmatrix} + \begin{bmatrix} \eta_n \\ \eta_s \\ \eta_a \end{bmatrix} \qquad (5)$$

$$\frac{d}{dt} x = Fx + \eta \qquad (6)$$

where, $\frac{d}{dt}$ is the differentiator operator with time t, F_n is the inertial navigator error model dynamic matrix, F_{ns} is the coupling matrix that implements the coupling of the inertial sensor errors into inertial navigator error model, F_s is the inertial sensor error dynamics matrix, Fa is the aiding sensor error model dynamics matrix which is random constant model in this case ($F_a = 0$) that represents the GNSS double differencing phase ambiguities dynamics (does not change from one epoch to another as along

Figure 3. The real-time KSACORS-based NRTK GNSS-INS integration scheme and post-processed KSACORS-based BPPK GNSS-INS integration scheme.

as no cycle slip exists), F is the full state model dynamic matrix, η is the state model noise. Klaman filter is implemented to estimate the error state vector $\hat{x}$ and associated covariance matrix $C_{\hat{x}\hat{x}}$ using the measurement model and state model. Then, the final navigation solution is the sum of the computed navigation solution from the inertial navigator $\hat{x}_{INS}$ and the inertial navigator error state vector $\hat{x}_n$ estimated from Klaman filter solution.

For KSACORS-based NRTK GNSS-INS Navigation solution, the real-time forward Kalman filter is implemented. However, for KSACORS-based NPPK GNSS-INS Navigation solution, the post-processed forward-backward smoother is implemented. The forward-backward smoother navigation solution is estimated as follows (Gelb 1974):

$$C_{\hat{x}_n\hat{x}_n}^S = \left(C_{\hat{x}_n\hat{x}_n}^F{}^{-1} + C_{\hat{x}_n\hat{x}_n}^B{}^{-1} \right)^{-1} \qquad (7)$$

$$\hat{x}_n^S = C_{\hat{x}_n\hat{x}_n}^S \left(C_{\hat{x}_n\hat{x}_n}^F{}^{-1}\hat{x}_n^F + C_{\hat{x}_n\hat{x}_n}^B{}^{-1}\hat{x}_n^B \right) \qquad (8)$$

where, $\hat{x}_n^S$ is the smoothed navigation solution, $C_{\hat{x}_n\hat{x}_n}^S$ is the covariance matrix associated with the smoothed navigation solution, $\hat{x}_n^F$ is the forward navigation solution, $C_{\hat{x}_n\hat{x}_n}^F$ is the covariance matrix associated with forward navigation solution, $\hat{x}_n^B$ is the backward navigation solution, $C_{\hat{x}_n\hat{x}_n}^B$ is the covariance matrix associated with back-ward navigation solution. The details of different GNSS-INS integration schemes and filters can be found in Gelb (1974) and Brown and Hwang (1997).

3. Methodology

To evaluate the KSACORS performance for coastal hydrographic surveying applica-tions, the real-time KSACORS-based NRTK GNSS-INS integration and post-proc-essed KSACOSR-based NPPK GNSS-INS integration solutions were investigated. Figure 3 shows the methodology implemented in this paper to evaluate the KSACORS performance in real-time and post-processed mode using positioning and attitude system that comprises dual GNSS system, for accurate positioning and heading solution, and Inertial Measurement System (IMU), for accurate attitude solu-tion. In real time mode, the KSACORS control center transmits a real-time NRTK_VRS GNSS data in RTCM format to the GNSS-MU system via NTRIP proto-col to provide NRTK GNSS-INS navigation solution. In post-processing mode, the GNSS observation files from multiple KSACORS stations (minimum recommended number of stations are four stations) are retrieved from the KSACORS website to be employed in creating a virtual SmartBase station in the survey area using Applanix POSPac tools software, where the GNSS data of the generated SmartBase is then employed to provide post-processed NPPK GNSS-INS navigation solution (Applanix 2017). It should be noted that the measurement component includes an inertial meas-urement unit (IMU), which consists of accelerometers, and gyros that can provide the essential acceleration and rotation information of the vessel, and a dual-frequency GPS receiver
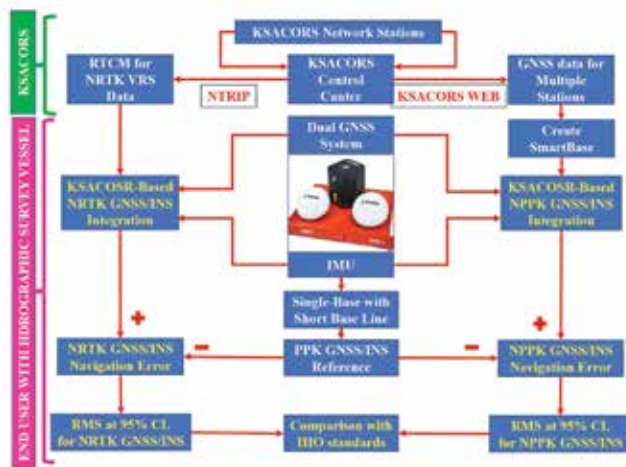
which can provide dual-frequency pseudo range, carrier phase and phase rate measurements. To investigate the accuracy performance of the two pro-posed integration schemes in this paper, a comparison is made between the proposed KSACORS-based NRTK GNSS-INS and NPPK GNSS-INS integration schemes, against the GNSS-INS navigation solution based on GNSS data collected by the single-base station with short baseline for the survey area that is considered as a "reference" solution, so called reference PPK GNSS-INS. Two RMS errors at 95%confidence level for 3D positions, roll, pitch and heading are estimated from the KSACORS-based NRTK GNSS-INS and NPPK GNSS-INS navigation solution when compared against reference PPK GNSS-INS navigation solution to investigate whether this navigation solution can meet the international standards (IHO standards) for hydrographic surveys. It should be noted that the GNSS-INS navigation solution pro-posed in this paper is carried out by POSPac tools software based on data collected from POS-MV system. In POSPac, a tightly coupled filter for GNSS-INS integration is employed to provides a more accurate solution when compared with a loosely coupled filter (Applanix 2017). The NRTK GNSS-INS navigation solution is investi-gated using the tightly coupled real-time forward Klaman filter solution. The NPPK GNSS-INS navigation solution is investigated using the tightly coupled post-processed forward-backward smoother solution from POSPac.

4. Multibeam surveying standards

The main objective of this paper is to evaluate the real-time KSACORS-based NRTK GNSS-INS integration and the post-processed KSACORS-based NPPK GNSS-INS integration navigation solution performance for coastal hydrographic surveying applications and then to investigate whether this navigation solution can meet the inter-national standards (IHO standards) for hydrographic surveys. The heave of the vessel must be measured to an accuracy of better than 0.05 m or 5% of the maximum heave to be consistent with the IHO standard. Heading error impacts the position error of each acoustic pixel. The acoustic pixel size represents the resolution of the bathymet-ric data and is selected by the hydrographer based on the type of the application, but it should not be less than the smallest acoustic pixel size that is a depth dependent.

In order to obtain a 0.5 m pixel position error in the outer beam of a ± 75° fan at a depth of 100 m, the heading error must be better

than 0.05°. On the other hand, the roll and the pitch errors cause both horizontal and vertical errors. Consequently, the roll and
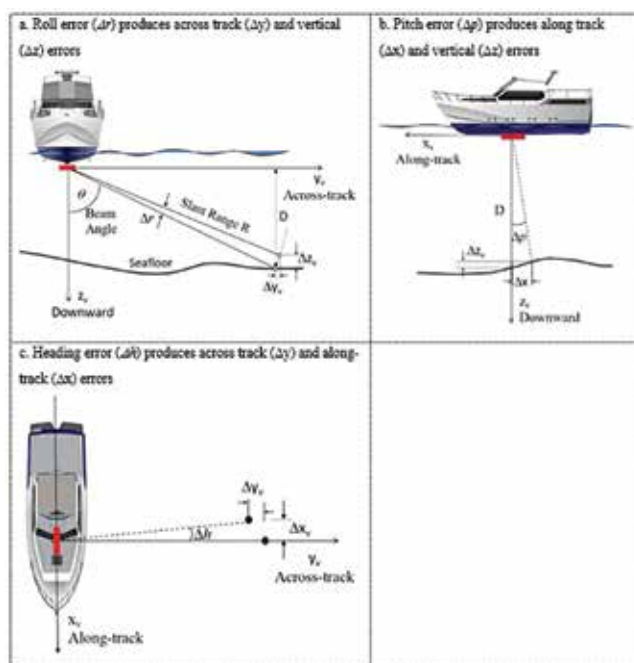

Figure 4. Schematic of the roll (Dr) error plot is shown in 4a, the pitch (Dp) error plot is shown in 4 b and heading (Dh) error plot is given in 4c.
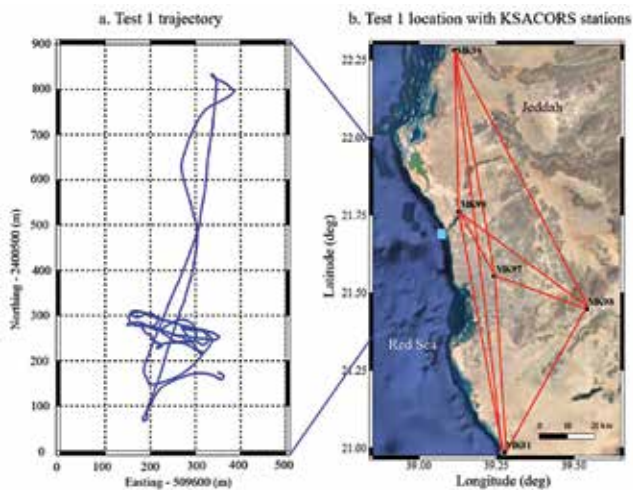

Figure 5. Test 1 trajectory (left panel) and location with KSACORS stations (right panel) for the approach area of Obhur Creek.

Table 1. IHO positioning and attitude (orientation) accuracy requirements at 95% confidence level.

Parameter/Order	Special order	Order 1a	Order 1b	Order 2
Horizontal position accuracy	2 m	5 m þ 5% of the depth	20 m þ 5% of the depth	150 mþ 5% of the depth
Depth accuracy	0.25-0.39 m (1-40 m depth)	0.5-1.39 m (1-100 m depth)	2.5-4.7 m (100-200 m depth)	Same as order 1b
Roll accuracy	0.10°	0.10°	0.10°	0.10°
Pitch accuracy	0.10°	0.10°	0.20°	0.20°
Heading accuracy	0.10°	0.10°	0.20°	0.20°

pitch of the vessel must be measured to an accuracy of better than 0.05° if the multibeam echosounder system of ±75° from nadir swath width is utilized. Therefore, the attitude parameters in all three axes (roll, pitch and heading) of the vessel must be measured to an accuracy of better than 0.05° if a high accuracy multi-beam echosounder system is utilized. Figure 4 shows the roll, pitch and heading errors and how these errors introduce depth, along-track and across-track errors. These limits are estimated upon the worst-case combination of biases and measure-ment noise. In summary, to achieve full utilization of a multibeam echosounder and satisfy IHO standards, the hydrographic surveying vessel must be measured at the 95% confidence level for accuracy as shown in Table 1 (Scherzinger 2005; IHO 2008; El-Diasty 2016).

5. Field test description

To examine the performance of the KSACORS-based NRTK GNSS-INS and NPPK GNSS-INS navigation solution for hydrographic surveying application, kinematic data from a dual frequency Trimble BD982 GNSS receiver and inertial data from a tactical-grade IMU (LN-200 by Northrop Grumman) were collected on April 17th, 2019 in Obhur Creek approach (test 1) and on November 14th, 2017 inside Obhur Creek (test 2) onboard a hydrographic surveying vessel called "KAU Hydrography 2" owned by the Department of Hydrographic Surveying, Faculty of Maritime Studies of King Abdulaziz University. Figures 5 and 6 show the test 1 and test 2 trajectories in Obhur Creek approach (mouse) and inside Obhur Creek, respectively, in Jeddah of Saudi Arabia that is located on Red Sea. In test 1 and test 2, two GNSS antennas were used to estimate the GPS heading, in addition to the GNSS position solution for updating the INS navigation solution to provide accurate GNSS-INS integrated navigation solu-tion. The reference station measurements at the roof of Faculty of Maritime Studies (spans about few kms from the moving rover stations) were simultaneously collected and employed to estimate the PPK GNSS-INS navigation solution and considered as the reference solution to validate the KSACORS-based real-time NRTK GNSS-INS and post-processed NPPK

Figure 6. Test 2 trajectory (left panel) and location with KSACORS stations (right panel) for the area inside Obhur Creek.

GNSS-INS navigation solutions. The real-time NRTK_VRS RTCM data were received by Applanix POSView acquisition software via NTRIP cli-ent with account authorized from GCS to provide real-time NRTK GNS/INS naviga-tion solution. Fore test 1 and test 2, five stations from KSACORS network were downloaded from KSACORS web to create virtual SmartBase station to provide post-processing NPPK GNS/INS navigation solution. Figures 5 and 6 shows the network of five stations that were employed to create virtual SmartBase station for test 1 and test 2 survey areas. The closest network GNSS stations to test 1 test 2 are about 8 km and 25 km, respectively. It is shown in Figures 5 and 6 that the network structure for test 1 and test 2 comprises four identical stations (MK01, MK96, MK97 and MK98), however, test 1 additionally comprises MK99 and test 2 additionally comprises MK93 based on the KSACORS GNSS data availability during the test time.

6. Results and discussion

The real-time KSACORS-based NRTK GNSS-INS, post-processed KSACORS-based NPPK GNSS-INS navigation solution and the reference post-processed PPK GNSS-INS navigation solution were obtained using the collected GNSS and IMU data measurements. Then, the performance of the developed real-time NRTK GNSS-INS and the post-processed NPPK GNSS-INS integrated systems were investigated whether it can meet the IHO standards for hydrographic surveys, particularly the horizontal pos-ition, roll, pitch and heading accuracies. Figures 7 and 8 show the position (north, east, height and 3D position) and attitude (roll, pitch, and heading) differences (errors) for test 1 between the position and attitude estimated from the real-time NRTK and NPPK GNSS-INS navigation solutions, respectively, and the position and attitude estimated from the "reference" PPK GNSS-INS integrated solution, where PPK is considered as a "reference" solution. Figures 9 and 10 show the position and attitude differences (errors) for test 2 between the position and attitude estimated from the real-time NRTK and NPPK GNSS-INS navigation solutions, respectively, and the position and attitude estimated from the "reference" PPK GNSS-INS inte-grated solution, where PPK is considered as a "reference" solution. Table 2 shows the 3D position and attitude errors summary statistical values estimated from the real-time NRTK and the post-processed NPPK GNSS-INS navigation solutions for test 1 and test 2 datasets. It can be seen from test 1 and test 2 summary statistics in Table 2 that the position accuracy estimated from the post-processed NPPK GNSS-INS navigation solutions (NPPK solutions of tests 1 and 2) based on 3D position RMS error (about 4 cm in average) outperforms the position accuracy estimated from the real-time NRTK GNSS-INS navigation solutions (NRTK solutions of tests 1 and 2) based on 3D position RMS error (about 7 cm in average). It can also be seen from test 1 and test 2 statistics that the attitude accuracy estimated from the post-processed NPPK GNSS-INS navigation solution (NPPK solutions of tests 1 and 2) based on atti-tude RMS error (about 0.015 arc-min in average) is significantly superior to the atti-
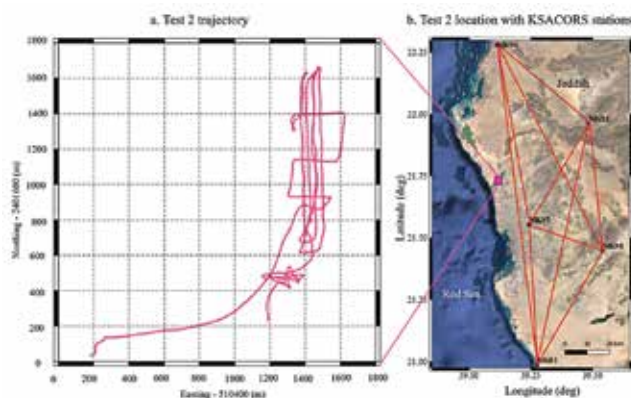
tude accuracy estimated from the real-time NRTK GNSS-INS navigation solution (NRTK solutions of tests 1 and 2) based on attitude RMS error (about 1.5 arc-min in average) with about two orders of magnitude. It should be noted that the position accuracy estimated from test 1 (NRTK and NPPK solutions) based on 3D position RMS error (about 4.5 cm in average) outperforms the position accuracy from test 2 (NRTK and NPPK solutions) based on 3D position RMS error (about 6.5 cm in aver-age) because the closest GNSS KSACORS station to test 1 is about 8 km and the clos-est GNSS KSACORS station to test 2 is about 25 km that makes the VRS station created in test 1 case closer to the survey area more than the VRS station created in test 2 case. It is also worth noting that the attitude solution estimated from test 2 (NRTK and NPPK solutions) based on attitude RMS error (about 0.4 arc-min in average) outperforms the attitude solution estimated from test 1 (NRTK and NPPK solutions) based on attitude RMS error (about 0.9 arc-min in average) because the test 2 survey area is located inside Obhur Creek which is considered low sea dynamic state (shallow area) with low orientation dynamic and produces less attitude errors, however, the test 1 survey area is located in Obhur Creek approach (mouse) which is considered high sea dynamic state (deeper and open area) with high orientation dynamic and produces high attitude errors.
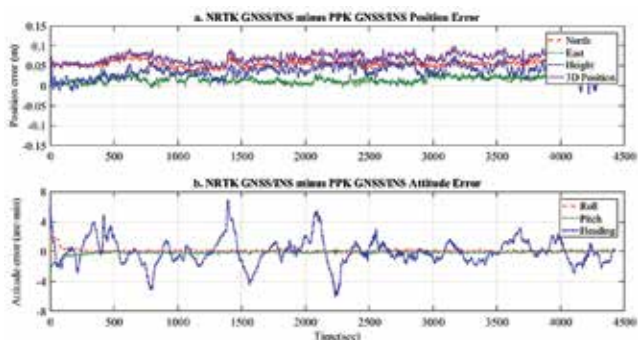
Now, the errors should be estimated at 95% confidence level as recommended by IHO. Figures 11 and 12 show the cumulative position (2D horizontal and vertical errors) and attitudes (roll, pitch and heading errors) errors distribution from the real-time NRTK and NPPK GNSS-INS navigation solutions of test 1 datasets, respectively, that show the majority of position and attitude errors at 95% confidence level from the real-time NRTK GNSS-INS navigation solution. Figures 13 and 14 show the cumulative position (2D horizontal and vertical errors) and attitudes (roll, pitch and heading errors) errors distribution from the real-time NRTK and NPPK GNSS-INS navigation solutions of test 2 datasets, respectively, that show the majority of position and attitude errors at 95% confidence level from the real-time NRTK GNSS-INS navi-gation solution. Figures 11–14 show that centimeters and arc-minutes level of accuracies at 95% confidence level can be successfully achieved for the position and attitude solutions, respectively, when KSACORS-based NRTK or NPPK GNSS-INS integration methods employed for hydrographic surveys applications in test 1 and test 2.

To estimate the overall RMS error, the differences (errors) between the KSACORS- based real-time NRTK GNSS-INSS and post-processed NPPK GNSS-INS integrated

Figure 7. Test 1 position errors (upper panel) and attitude errors (lower panel) estimated from the difference between the KSACORS–based real–time NRTK GNSS–INS navigation solution and the refer–ence PPK GNSS–INS navigation solution.
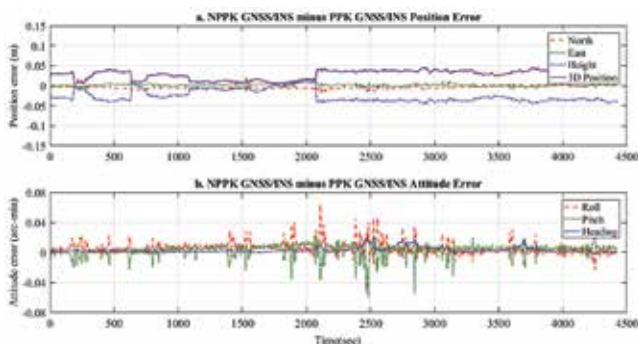

Figure 8. Test 1 position errors (upper panel) and attitude errors (lower panel) estimated from the difference between the KSACORS–based post–processed NPPK GNSS–INS navigation solution and the reference PPK RTK–based navigation solution.
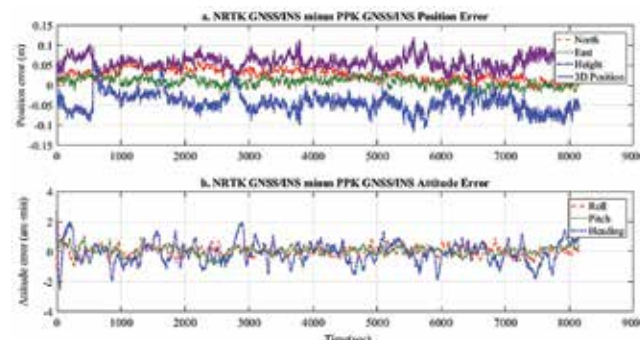

Figure 9. Test 2 position errors (upper panel) and attitude errors (lower panel) estimated from the difference between the KSACORS–based real–time NRTK GNSS–INS navigation solution and the refer–ence PPK GNSS–INS navigation solution.
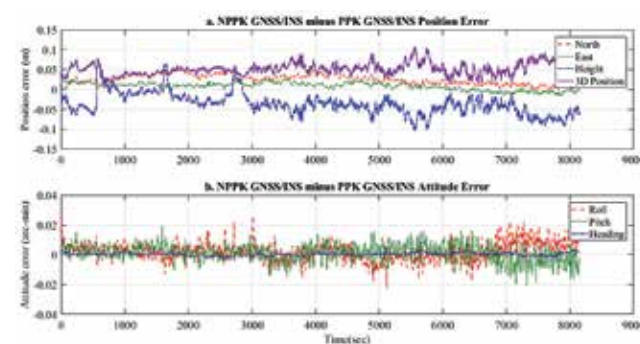

Figure 10. Test 2 position errors (upper panel) and attitude errors (lower panel) estimated from the difference between the KSACORS–based post–processed NPPK GNSS–INS navigation solution and the reference PPK RTK–based navigation solution.

Table 2. The 3 D position and attitude errors summary statistical values estimated from the real-time NRTK and the post-processed NPPK GNSS-INS navigation solutions of test 1 and test 2 data sets.

Test		Test 1		Test 2	
Parameter	Solution	NRTK	NPPK	NRTK	NPPK
3D Position	Min	3.9 cm	0.4 cm	0.3 cm	1.5 cm
	Max	9.8 cm	4.6 cm	12.5 cm	10.7 cm
	RMS error	6.7 cm	3.0 cm	7.0 cm	5.5 cm
Attitude	Min	0.03 arc-min	0.01 arc-min	0.02 arc-min	0.01 arc-min
	Max	7.00 arc-min	0.07 arc-min	3.00 arc-min	0.03 arc-min
	RMS	1.80 arc-min	0.02 arc-min	0.83 arc-min	0.01 arc-min

Figure 11. Test 1 cumulative distribution for position errors and attitude errors that shows the majority of position error and attitude error at 95% confidence level from the real-time NRTK GNSS-INS navigation solution.

Figure 13. Test 2 cumulative distribution for position errors and attitude errors that shows the majority of position error and attitude error at 95% confidence level from the real-time NRTK GNSS-INS navigation solution.

Figure 12. Test 1 cumulative distribution for position errors and attitude errors that shows the majority of position error and attitude error at 95% confidence level from the post-processed NPPK GNSS-INS navigation solution.
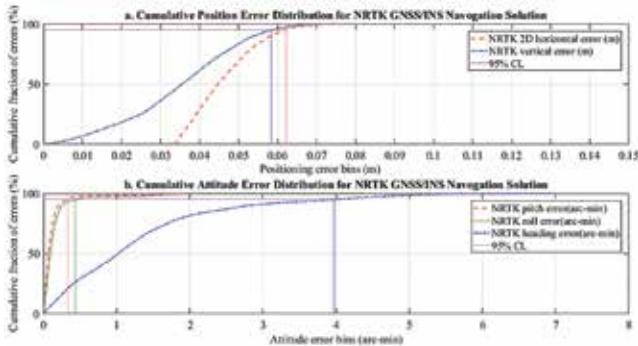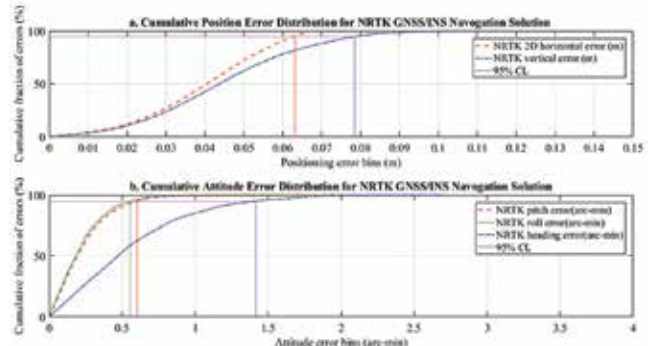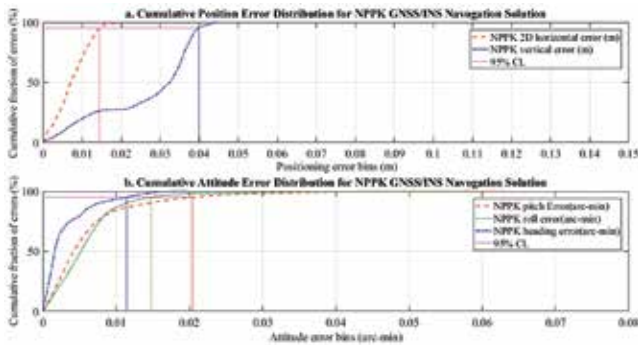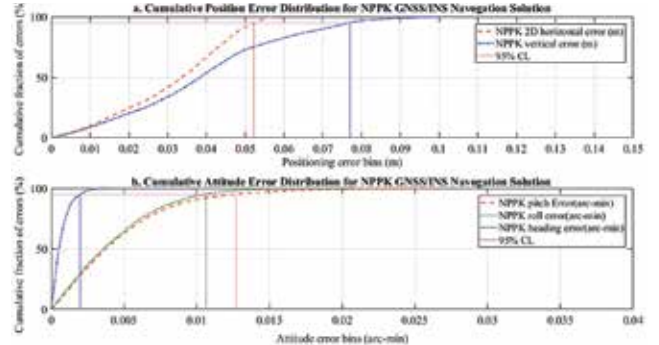

Figure 14. Test 2 cumulative distribution for position errors and attitude errors that shows the majority of position error and attitude error at 95% confidence level from the post-processed NPPK GNSS-INS navigation solution.

Table 3. Test 1 overall accuracy (RMS) of the real-time KSACORS-based NRTK GNSS-INS integrated system (at 95% CL).

Error parameter	RMS_{PPK} at 95% CL	$RMS_{NRTK-PPK}$ at 95% CL	RMS_{NRTK} at 95% CL
2D Horizontal accuracy	0.045 m	0.062 m	0.08 m
Vertical accuracy	0.05 m	0.058 m	0.08 m
Roll accuracy	0.03°	0.015°	0.04°
Pitch accuracy	0.03°	0.014°	0.04°
Heading accuracy	0.06°	0.070°	0.09°

solutions with the PPK GNSS-INS reference solution are utilized in the following form as (El-Diasty 2016):

$$RMS_{NRTK} = \sqrt{RMS_{NRTK-PPK}^2 + RMS_{PPK}^2} \qquad (9)$$

$$RMS_{NPPK} = \sqrt{RMS_{NPPK-PPK}^2 + RMS_{PPK}^2} \qquad (10)$$

Table 4. Test 1 overall accuracy (RMS) of the post-processed KSACORS-based NPPK GNSS-INS inte-grated system (at 95% CL).

Error parameter	RMS_{PPK} at 95% CL	$RMS_{NPPK-PPK}$ at 95% CL	RMS_{NPPK} at 95% CL
2D Horizontal accuracy	0.045 m	0.015 m	0.05 m
Vertical accuracy	0.05 m	0.04 m	0.06 m
Roll accuracy	0.03°	0.002°	0.03°
Pitch accuracy	0.03°	0.003°	0.03°
Heading accuracy	0.06°	0.002°	0.06°

Table 5. Test 2 overall accuracy (RMS) of the real-time KSACORS-based NRTK GNSS-INS integrated system (at 95% CL).

Error parameter	RMS_{PPK} at 95% CL	$RMS_{NRTK-PPK}$ at 95% CL	RMS_{NRTK} at 95% CL
2D Horizontal accuracy	0.045 m	0.063 m	0.08 m
Vertical accuracy	0.05 m	0.078 m	0.09 m
Roll accuracy	0.03°	0.012°	0.04°
Pitch accuracy	0.03°	0.011°	0.04°
Heading accuracy	0.06°	0.03°	0.07°

Table 6. Test 2 overall accuracy (RMS) of the post-processed KSACORS-based NPPK GNSS-INS inte-grated system (at 95% CL).

Error parameter	RMS_{PPK} at 95% CL	$RMS_{NPPK-PPK}$ at 95% CL	RMS_{NPPK} at 95% CL
2D Horizontal accuracy	0.045 m	0.052 m	0.07 m
Vertical accuracy	0.05 m	0.077 m	0.09 m
Roll accuracy	0.03°	0.001°	0.03°
Pitch accuracy	0.03°	0.001°	0.03°
Heading accuracy	0.06°	0.0001°	0.06°

where RMS_{NRTK} is the best estimates of the root-mean-square error of the KSACORS-based real-time NRTK GNSS-INSS integrated solution, $RMS_{NRTK-PPK}$ is the estimated root-mean-square error of the actual error difference of the real-time NRTK GNSS-INS integrated solution when compared against reference PPK GNSS-INS integrated solution, RMS_{PPK} is the best estimates of the root-mean-square error of the "reference" PPK GNSS-INS integrated solution, RMS_{NPPK} is the best estimates of the root-mean-square error of the KSACORS-based post-processed NPPK GNSS-INSS integrated solution and $RMS_{NPPK-PPK}$ is the estimated root-mean-square error of the actual error difference of the post-processed NPPK GNSS-INS integrated solu-tion when compared against reference PPK GNSS-INS integrated solution.

Tables 3 and 4 show the test 1 root-mean-square errors (overall accuracy -RMS_{NRTK} and RMS_{NPPK}) for 2D horizontal position, vertical position, roll, pitch and heading at 95% confidence level estimated based on Equations 9 and 10 using the real-time KSACORS-based NRTK and NPPK GNSS-INS navigation solutions, respectively. Tables 5 and 6 show the test 2 root-mean-square errors (overall accuracy -RMS_{NRTK} and RMS_{NPPK}) for 2D horizontal position, vertical position, roll, pitch and heading at 95% confidence level estimated based on Equations 9 and 10 using the real-time KSACORS-based NRTK and NPPK GNSS-INS navigation solutions, respectively. Tables 7–10 show test 1 and test 2 root-mean-square errors (overall accuracy) of the evaluated real-time KSACORS-based NRTK GNSS-INS integrated navigation solutions and the evaluated post-processed KSACORS-based NPPK GNSS-INS inte-grated navigation solutions, respectively, against the IHO special order requirements for horizontal position, vertical position, roll, pitch, and heading at 95% confidence level. It should be noted from Tables

7–10 that the IHO vertical positioning accuracy ranges from 20% to 60% of the total depth error listed in Table 1 when the tide is estimated from the GNSS-INS integrated system (called GNSS tide) in hydrographic of the evaluated real-time KSACORS-based NRTK GNSS-INS integrated navigation solutions and the evaluated post-processed KSACORS-based NPPK GNSS-INS inte-grated navigation solutions, respectively, against the IHO special order requirements for horizontal position, vertical position, roll, pitch, and heading at 95% confidence level. It should be noted from Tables 7–10 that the IHO vertical positioning accuracy ranges from 20% to 60% of the total depth error listed in Table 1 when the tide is estimated from the GNSS-INS integrated system (called GNSS tide) in hydrographic data processing workflow (Van Norden et al. 2008; El-Diasty 2016). It is shown from Tables 7–10 that the evaluated real-time KSACORS-based NRTK GNSS-INS naviga-tion solution accuracies and the evaluated post-processed KSACORS-based NPPK GNSS-INS navigation solution accuracies at 95% confidence level for test 1 and test 2 fulfill the IHO order special order for 2D horizontal position, vertical position, roll, pitch and heading standards at 95% confidence level. Consequently, the IHO order 1a, IHO order 1 b and order 2 requirements (shown in Table 1) are fully fulfilled with the evaluated NRTK and PPK GNSS-INS integrated solutions. Therefore, it is concluded that the evaluated real-time KSACORS-based NRTK GNSS-INS integrated solution and the evaluated post-processed KSACORS-based NPPK GNSS-INS inte-grated solution can fulfill the IHO requirements for all orders. It was found from test 1 and test 2 results that the vertical accuracy is considered as the most stringent IHO standard requirement and accurate GNSS-INS vertical solution is required. It is worth noting that as far as the multibeam survey area is located far in distance from the shore and consequently far in distance from KSACORS stations, the KSACORS-based GNSS-INS vertical solution accuracy becomes less, however, the IHO standard verti-cal requirement become less

Table 7. Test 1 real-time KSACORS-based NRTK GNSS-INS integrated system against IHO special order standards.

Error parameter	IHO Requirements at 95% CL (special order)	Real-time KSACORS-based NRTK GNSS-INS method	
		RMS_{NRTK} at 95% CL	Satisfy IHO standards
2D Horizontal positioning accuracy	2.0	0.08 m	Yes
Vertical positioning accuracy	0.13-0.20 m (1-40 m depth)	0.08 m	Yes
Roll Accuracy	0.098°	0.04°	Yes
Pitch accuracy	0.098°	0.04°	Yes
Heading accuracy	0.098°	0.09°	Yes

Table 8. Test 1 post-processed KSACORS-based NPPK GNSS-INS integrated system against IHO special order standards.

Error parameter	IHO Requirements at 95% CL (special order)	Post-processed KSACORS-based NPPK GNSS-INS method	
		RMS_{NPPK} at 95% CL	Satisfy IHO standards
2D Horizontal positioning accuracy	2.0	0.05 m	Yes
Vertical positioning accuracy	0.13-0.20 m (1-40 m depth)	0.06 m	Yes
Roll Accuracy	0.098°	0.03°	Yes
Pitch accuracy	0.098°	0.03°	Yes
Heading accuracy	0.098°	0.06°	Yes

Table 9. Test 2 real-time KSACORS-based NRTK GNSS-INS integrated system against IHO special order standards.

Error parameter	IHO Requirements at 95% CL (special order)	Real-time KSACORS-based NRTK GNSS-INS method	
		RMS_{NRTK} at 95% CL	Satisfy IHO standards
2D Horizontal positioning accuracy	2.0	0.08 m	Yes
Vertical positioning accuracy	0.13-0.20 m (1-40 m depth)	0.09 m	Yes
Roll Accuracy	0.098°	0.04°	Yes
Pitch accuracy	0.098°	0.04°	Yes
Heading accuracy	0.098°	0.07°	Yes

Table 10. Test 2 post-processed KSACORS-based NPPK GNSS-INS integrated system against IHO special order standards.

Error parameter	IHO Requirements at 95% CL (special order)	Post-processed KSACORS-based NPPK GNSS-INS method	
		RMS_{NPPK} at 95% CL	Satisfy IHO standards
2D Horizontal positioning accuracy	2.0	0.07 m	Yes
Vertical positioning accuracy	0.13-0.20 m (1-40 m depth)	0.09 m	Yes
Roll Accuracy	0.098°	0.03°	Yes
Pitch accuracy	0.098°	0.03°	Yes
Heading accuracy	0.098°	0.06°	Yes

stringent where it is respectively reduced in order classi-fication from special order to lower orders as shown in Table 1.

7. Conclusion and recommendation

This paper evaluated a real-time KSACORS-based NRTK GNSS-INS integrated solu-tion and a post-processed KSACORS-based NPPK GNSS-INS integrated solution and then investigated whether these methods can meet the international standards (IHO standards)

for hydrographic surveys performed by multibeam echosounder. It is shown that the real-time KSACORS-based NRTK GNSS-INS integrated solution and the post-processed KSACORS-based NPPK GNSS-INS integrated solution accuracies for horizontal position, vertical position, roll, pitch and heading can fulfill the IHO special order, order 1a, order 1b and order 2 requirements at 95% confidence level. The significance of the evaluated real-time that the real-time KSACORS-based NRTK GNSS-INS integrated system model and the post-processed KSACORS-based NPPK GNSS-INS integrated

system model is that they introduced an alternative, inexpensive navigation solution to the traditional PPK GNSS-INS system model that requires a dedicated single-base station where these methods employed the free of charge KSACORS products delivered to the end user in real time and post-processed modes.

However, it is recommended to employ the real-time KSACORS-based NRTK or post-processed NPPK GNSS.INS integrated methods for hydrographic survey for an area within a KSACORS baseline limit of 70 km to the nearest

onshore KSACORS station if accurate navigation solution at centimeters level of accuracy is required.

Acknowledgements

References

Alomar A, Yanar R, Albalawi S, Alzahrani S. 2018. The Kingdom of Saudi Arabia GNSS real-time kinematic network (MRTN) and beyond (a case study for high accuracy vrs correction test). FIG Congress, Istanbul, Turkey, 6–11 May, 2018.

Applanix. 2017. POSPac MMS GNSS-Inertial Tools Software. Richmond Hill, Canada: Applanix Corporation.

Brown RG, Hwang P. 1997. Introduction to random signals and applied kalman filtering. Toronto, Canada: John Wiley & Sons, Inc.

El-Diasty M. 2010. Development of a MEMS-based INS/GPS vessel navigation system for marine applications [PhD dissertation]. Toronto (Canada): York University.

El-Diasty M. 2016. Development of real-time PPP-based GPS/INS integration system using IGS real-time service for hydrographic surveys. J Surv Eng. 142(2):05015005. pp

GCS. 2019. KSA-continuous operation reference station network. [accessed 2019 Nov]. https://ksacors.gcs.gov.sa/. Gelb

A. 1974. Applied optimal estimation. Cambridge, MA: The MIT Press.

Golubinka L. 2018. GCS (General Commission for Survey, Riyadh, KSA) Data & Analysis Centre – the results of processing the data from GNSS CORS network. IGS Workshop pos-ter, IGS Workshop,

Hofmann-Wellenhof B, Lichtenegger H, and E. Walse. 2008. GNSS global navigation satellite systems; GPS, glonass, galileo & more. New York: Springer-Verlag Wien.

Hutton J, Alan A, Bourke T, Scherzinger B, Gopaul N, Canter P, Ovel I, Blankenberg L. 2008. Tight integration of GNSS post-processed virtual reference station with inertial data for increased accuracy and productivity of airborne mapping. Remote Sens Spatial Inform Sci. 37(Part B5): 15–16.

Hutton J, Bourke T, Scherzinger B. 2007. New developments of inertial navigation systems at Applanix. Photogrammetric Week'07; p. 201–213.

IHO (International Hydrographic Organization Committee). 2008. IHO Standards for Hydrographic Surveys. 5th ed., Special Publication No. 44, MONACO: International Hydrographic Bureau.

Landau H, Vollath U, Chen X. 2002. Virtual reference station systems. J Global Position Syst. 1(2):137–143.

Retscher G. 2002. Accuracy performance of virtual reference station (VRS) networks. J Global Position Syst. 1(1):40–47.

Rizos C, Han S. 2003. Reference station network based RTK systems – concepts and progress. Wuhan Univ J Nat Sci. 8(2):566–574. No

Scherzinger BM. 2000. Precise robust positioning with inertial/GPS RTK. Proceedings of GPS- 2000, The Institute of Navigation, Alexandria, VA; p. 155–162.

Scherzinger BM. 2002. Robust positioning with single frequency inertially aided RTK. Proceeding of ION NTM'02, San Diego, CA; p. 911–917.

Scherzinger BM. 2005. Economics of INS/GPS integration for survey applications. Proceedings of the 52nd CASI Conference, Toronto, Canada, April 26.

Tusat E. 2018. A comparison of the accuracy of VRS and static GPS measurement results for production of topographic map and spatial data: a case study on CORS-TR. Tech Gaz. 25(1): 158–163.

Ulrich V, Alois A, Herbert L, Christian P, Bernhard W. 2000. Long-Range RTK Positioning Using Virtual Reference Stations. Proceedings of the 13th International Technical Meeting of the Satellite Division of The Institute of Navigation (ION GPS 2000), Salt Lake City, UT, September 2000; p. 1143–1147.

Van Norden MF, Ladner, RW. Arroyo-Suarez EN. 2008. Developing a concept of operations for military surveys to IHO standards without shore-based stations. Proceedings of the Canadian Hydrographic Conference and National Surveyors Conference.

Wei E, Chai H, An Z, Liu J. 2006. VRS virtual observations generation algorithm. J Global Position Syst. 5(1–2):76–81.

Mapping the urban atmospheric carbon stock

Readers may recall that we have published the first part of this paper in April 2022 issue of Coordinates where material and methods were discussed. Here we present the concluding part

MD Abdul Mueed Choudhury

Department of Agricultural, Food, and Environmental Sciences, Marche Polytechnic University, 60131 Ancona, Italy

Ernesto Marcheggiani

Department of Agricultural, Food, and Environmental Sciences, Marche Polytechnic University, 60131 Ancona, Italy
Division of Forest, Nature, and Landscape, Department of Earth and Environmental Sciences, KU Leuven, 3001 Leuven, Belgium

Andrea Galli

Department of Agricultural, Food, and Environmental Sciences, Marche Polytechnic University, 60131 Ancona, Italy

Giuseppe Modica

Dipartimento di Agraria, Università degli Studi Mediterranea di Reggio Calabria, Località Feodi Vito, 89122 Reggio Calabria, Italy

Ben Somers

Division of Forest, Nature, and Landscape, Department of Earth and Environmental Sciences, KU Leuven, 3001 Leuven, Belgium

3. Results

3.1. GEOBIA Classification Results and Validation

As the WV-3 image was from the early spring, trees having dead leaves/ branches made it relatively harder to identify the species in Brussels. Thus, species detection was difficult due to the spectral similarities and understory issues. However, the classified map shows that most of the streets are covered with the *Acer* spp. and *Tilia* spp., while the other species, *Aesculus hippocastanum* has been primarily observed in the southern part of the city (Figure 5).

The producer and user accuracy were around 70% for *Tilia* spp. and *Aesculus hippocastanum*, and around 80% to 100% were for the *Acer* spp. during the confusion matrix estimation (Table 2). Indeed, it was quite essential to define the effectiveness of the GEOBIA approach and to show the percentage of error.

3.2. CS Mapping and Validation

3.2.1. CS Mapping in Brussels with WV-3 Image Data

The computed CS for the dominant species has been mapped showing the quantity of CS based on the species in different zones (Figure 6). As far as most of the trees were on the streets, the canopies were not overlapped by the wider crowns. Except for some plots having trees almost leafless or trimmed canopies, the computed CS values based on NDVI derived variables were significant (Figure 6) for most of the dominant species.

Figure 6. Mapping outcomes of the computed Carbon Stocks (CS) for the dominant tree species (Acer spp., Aesculus hippocastanum, and Tilia spp.) superimposed over the NDVI map in the urban area of Brussels utilizing the WorldView-3 (WV- 3) image data (QGIS-NDVI).

In Figure 6, all three-square boxes (as in CS1, CS2, and CS3) are showing moderate (i.e., pink, orange, yellow, and blue coloured zones) to a higher quantity of CS for each of the species (as in TC1, TC2, and TC3). These three zones were zoomed-in considering those plots having comparatively dense canopies, as the WV-3 image was acquired in early spring, most of the plots were with lighter crowns or leaves.

In Table 3, the validation results show that the field estimation and QGIS computed CS values have apparent variations in few cases. These kinds of differences between the field estimated and the computed values were quite natural in the case of this study. The field data were collected in the summer of 2019, while the WV-3 image was acquired in the early spring of 2017. QGIS computation was done based on the NDVI (WV-3 data) extracted values where most of the trees were leafless or less green. As a result, in the case of few plots, NDVI values were lower, which indeed showed lower CS values during the mapping. In addition, the year gap between the field data (2019) and the WV-3 data (2017) also significantly impacted the CS mapping outcomes, since trees in urban areas usually go through the management practices (i.e., trimming, pruning, etc.) [146], which is also responsible for the larger variations among the field and QGIS computed values (Table 3). For instance, out of the 20 validation plots, only three plots (plot no. 4, 11, and 18) are showing noticeably more CS/plot than

those of the field estimations. Trees in those plots are assumed to be a subject of trimming and or other management practices, explaining the reasons for having lower AGB or CS/plot in 2019 than those of 2017 for those three plots. A regression analysis had been done to understand the significance of the mapping approach.

It was quite noticeable that in most cases where the tree canopies were comparatively evident, even in the early spring season, the percentage of agreement (Figure 7) was more than 80% (R2 = 0.83). Except for a few cases, this CS mapping approach could be applied in CS mapping, even in a complex urban environment.

3.2.2. CS Mapping in Brussels with LiDAR Data

Figure 8 shows that the computed CS map in QGIS was quite relevant in LiDAR data for all the identified dominant species

Figure 7. Linear correlation between field estimations and QGIS computations during the validation of the Carbon Stocks (CS) mapping in Brussels.
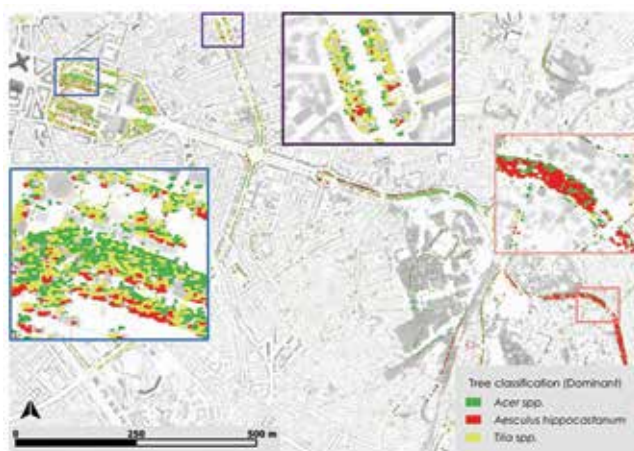

Figure 5. The figure shows the tree species classification (*Acer* spp., *Aesculus hippocastanum*, and *Tilia* spp.) obtained with the Geospatial Object–Based Image Analysis (GEOBIA) approach utilizing the WorldView–3 (WV–3) image data in the urban area of Brussels.
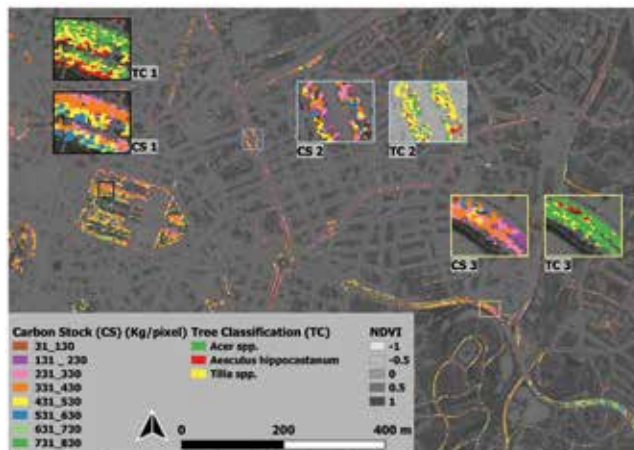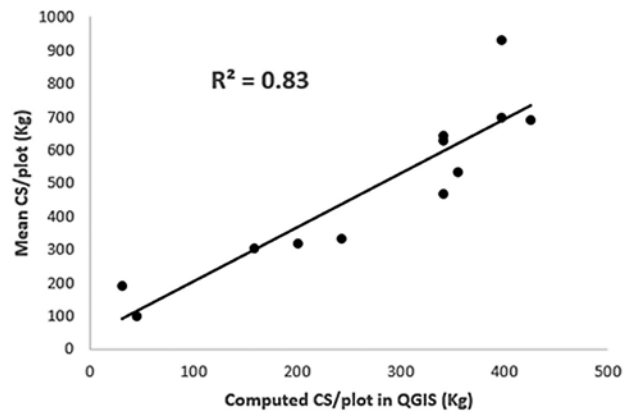

Figure 8. Mapping outcomes of the computed Carbon Stocks (CS) for the dominant tree species (*Acer* spp., *Aesculus hippocastanum*, and *Tilia* spp.) superimposed over the CHM LiDAR map in the urban area of Brussels (QGIS– CHM).
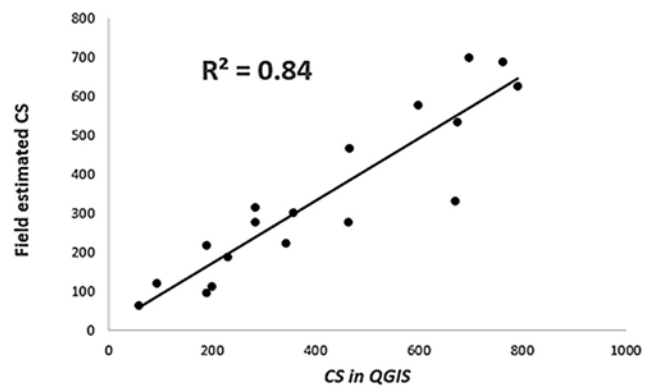

Figure 6. Mapping outcomes of the computed Carbon Stocks (CS) for the dominant tree species (*Acer* spp., *Aesculus hippocastanum*, and *Tilia* spp.) superimposed over the NDVI map in the urban area of Brussels utilizing the WorldView–3 (WV–3) image data (QGIS–NDVI).
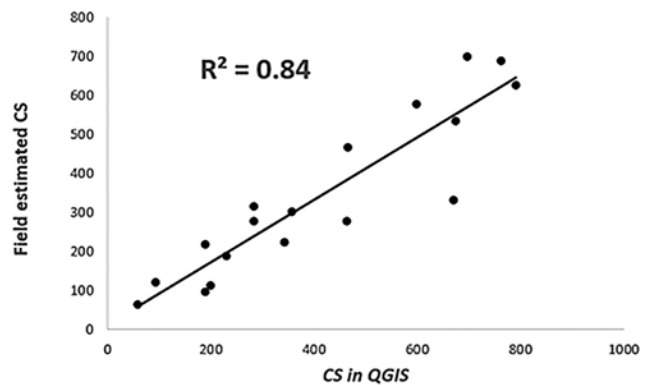

Figure 9. Linear correlation between field estimation and QGIS computation of CS/plot during the validation.

(TC1, TC2, and TC3 in Figure 8). Even the LiDAR data was from 2015, each of the three dominant species had shown evident outcomes in CS mapping (CS1, CS2, and CS3 in Figure 8) based on the field data of 2019. As the LiDAR data (from summer 2015) and field data were acquired in summer, the AGB productions per plots were significant to predict the CS during the mapping based on the CHM- derived variables in QGIS.

For the CS mapping validation, the validation plots were the same ones as earlier in the case of WV-3 image data. The outcomes of the validation plots did not show that much difference between the field estimated and QGIS computed values (Table 4). Only a few plots were showing higher differences in the quantity of computed CS, which was assumed to be a result of tree crown management practices (i.e., trimming, pruning, etc.) [146]. Out of all 20 plots, only a few plots (i.e., plot no. 2, 9, 14, 15, and 17) were showing noticeable variations between the field and QGIS estimations (Table 4). While in most of the plots, trees were showing lower differences in the case of the total atmospheric CS considering the on-plot calibrated values.

A regression analysis was done to understand the relevance of the applied CS mapping approach. It was noticed that the R2 was significantly higher (84%), for most of the plots (Figure 9). As shown earlier (Section 3.2.1), the data acquisition period (2015 and 2019) and the certain tree crown management practices (i.e., Trimming, pruning, etc.) [146] have also been found responsible for having larger variations in a few cases. As a result of regular crown trimming practices, the trees, even with a wider trunk, were showing smaller crowns in CHM during the CS computation in QGIS.

4. Discussion

4.1. GEOBIA Classification and Urban Trees

WV-3 image data were utilized to classify three dominant tree species applying the GEOBIA approach in the case of a heterogeneous urban area like as Brussels. The Overall Accuracy (OA) of the species classification was around 71%, considering all the identified urban tree species (Table 2). The classification accuracy could be improved (around 90%) by applying the data fusion (i.e., LiDAR and hyperspectral) approach or estimating OA considering the general urban land cover classification [147–153]. Since this study's primary goal was to identify and classify only the dominant tree species for further CS mapping in QGIS, we show the OA only referring to the trees class and not for the other land cover classes such as roads, grasslands, and pavements. Unfortunately, studies on urban tree species or genera-based classification (only with multispectral data) with better accuracy (more than 70%) are hardly available unless the study area is quite smaller (i.e., [154–156]).

Recently, Fang et al. [157] have done the tree genera-based classification (from WV-3 data) with an OA of 62 to 74% for a larger urban area in Washington D.C., USA. Considering a study area covering almost 49 km^2, this study in Brussels also could be a good example for approving the efficacy of the GEOBIA approach. The accuracy level was different for each species, where the higher was for the *Acer* spp. (89%) and the lower one was found for the *Aesculus hippocastanum* (64%). Initially, the segmentation and later the relevant samples for training the NN algorithm significantly influenced the OA of the classification outcomes, as shown in previous studies [36,158]. Training samples must be sufficient considering each species/class, which will be enough for the algorithm to verify different classes. In this study, the samples had been selected to train the NN algorithm covering the whole study area in Brussels. However, the different species' spectral characteristics made it quite challenging to distinguish due to their unique phenological ages or conditions [147,159]. In some cases, misinterpretations of desired classes had been identified, recognizing the "mixed pixel issues" where some pixels were not solely covered by one homogeneous class [147,160].

Consequently, with an OA of 71%, this study does show that the WV-3 data could be more convenient, especially in urban areas, as the WV-3 image has an increased level of radiometric, geometric, and spatial (8 bands) resolution leading to classify urban trees at the species level [147,161].

Even remote sensing-based technologies are far better acceptable, the potential barriers to adopting remote sensing techniques include but are not limited to the level of specialist knowledge, the data collection time, instruments type and parameters for the acquisitions, etc. For instance, the classification OA could minimize such issues as the image registration error, the spectral and spatial resolution limitations, and overlapping spectral signature of the classes. These facts could be considered to initiate further research to improve and utilize the GEOBIA approach to achieve a species-level classification with higher accuracy, especially for the urban trees.

4.2. CS Mapping Approach: A Comparative Analysis

In this study, the mapping approach has been found far more convincing than that of the existing traditional approaches (i.e., approaches excluding remote sensing tools). The traditional biomass assessment methods are mostly based on field measurements which are not so convenient or practical to conduct over large areas considering a broadscale assessment [8,162]. Considering the dominant species, the CS mapping outcomes in Brussels were quite explicit and feasible, where the assessment was highly influenced by the seasonal variations between the data sources (field and remote sensing data). However, no such factors or issues could hardly be sorted out to improve the mapping outcomes in both cases. For instance, it is evident that in Brussels, the CS mapping outcomes could be more significant having both data sources (i.e., field and remote sensing data) from the same season or year. The CS computation utilizing the LiDAR data could be a good example since there was not much variation with

the field estimations (Table 4). However, in all cases, there were other noticeable issues such as the narrow or too wide and/or small overlapped crowns, trimmed crowns, and so on other management practices. These issues are obvious to be considered precisely for any urban landscapes [7,63,64] that are heterogeneous in space, structurally, and functionally [44,163–165]. However, the proposed remote sensing-based methodology could be availed as more essential and applicable in the case of monitoring and mapping vegetation ecosystems and their services than that of the traditional ones.

To date, it is critical to developing a high-resolution map of tree biomass within the context of carbon monitoring over terrestrial ecosystems to assess the ecosystem response to climate change [166–171], which increases the utilization of RS-based technologies for the last few decades. For instance, LiDAR data are widely being used to complete high-resolution surveys of vegetation structure over forested areas and cities [53,172–175] and estimate biomass and carbon storage in urban vegetation [26,53,176,177] due to its im-proved accuracy. Even though it is believed that the application of RS is quite expensive in vegetation mapping, Jones et al. (2010) [33,178] found automated methods from combined hyperspectral and LiDAR data (approximately USD 6 per ha) to be competitive against traditional aerial photograph interpretation (approximately USD 12 per ha) in terms of accuracy and cost for a study area in South-western Canada. However, the availability of LiDAR data is not always cost-effective, especially for developing countries. For those cases where LiDAR data are hardly available, high-resolution image data could be a solution for the city policymakers. For instance, studies show that high-resolution commercial data (Rapid Eye, IKONOS, Geo-eye) are available with an approximate cost of 1–14 € per km2, which is still more affordable than the LiDAR data (USD 62–240 per km2) [179,180]. Ac-cording to Hummel et al., the approximate cost of aerial LiDAR data acquisition for an area of almost 128 km2 (31,614 acres) was around USD 40,500, excluding the

This mapping approach could be an efficient tool in CS mapping that will assist urban planners in ensuring proper utilization of the available green spaces considering other valuable prospects of tree species mapping in a complex city environment.

processing costs (additional USD 33,424) [181]. While the WV-3 image data covering an area of 128 km2 could be around USD 2500 (USD 19 km−2), considering the best possible buying options for archive imagery [182]. This could be an appropriate example of LiDAR data's application of almost 15 to 20 times higher than that of the WV-3 image data. Therefore, it could be a better initiative to imply other data sources, especially in developing countries, where it is impossible to integrate or have an available LiDAR data source. Considering the cost-efficiency and the research perspectives, this study has been conducted to identify the best outcomes in each case (LiDAR and WV-3 image data) and understand the result discrepancies among similar study areas. However, it is also clear that the mapping out-comes utilizing LiDAR data were more impressive (Table 4) than that of the WV3 data. Nevertheless, the regression analysis still showed a significant level of acceptance (Figure 7) for the WV-3 image outcomes in Brussels. On the other hand, the percentage of LiDAR data outcomes except for only a few plots was more than 80% (Figure 9).

Moreover, city planners and managers usually plan to rely on a few urban tree at-tributes i.e., urban forest structure, green cover, species composition and diversity, available planting spaces, and tree condition to make short- and long-term decisions about the urban forest resource [15]. However, at the same time, the costs associated with data collection and monitoring (such as remote sensing applications) have to be compensated by reducing field measurement expenses or increasing management efficiency that leads to increased income based on improved decision-making [33]. Therefore

the utilization and application of the advanced remote sensing technology depend on the purpose, economic feasibility, and the prospects of the resulted outcomes. Nevertheless, the proper understanding of the urban tree species contributions in atmospheric carbon sequestration and storage is one the most pertinent issues for urban green planning and management [183,184].

5. Conclusions

This mapping approach could be an efficient tool in CS mapping that will assist urban planners in ensuring proper utilization of the available green spaces considering other valuable prospects of tree species mapping in a complex city environment. This study will also recognize the prospects of the applied approach based on an efficient GEOBIA classification method for urban tree species mapping. For instance, this study shows that the OA of tree species classification could be hugely influenced by the trees' positions, crown structures, and spectral attributes, where the resulting outcomes were useful for further CS mapping in Brussels. The CS mapping approach reveals that the tree stands level and temporal variations of the data acquisition period might significantly impact the total atmospheric CS for each species in urban areas. This study highlights that accurate tree CS mapping is crucial for estimating and identifying the dominant species contributing a significant level of atmospheric CS, which could be an efficient support for the urban planners and environmental policymakers in planning further urban air quality assessments. It also illustrates the facts considering the

This study will contribute to a better understanding of the methodology in mapping structural and functional properties, such as tree CS, as well as predicting the possible urban CS in typical city areas. It might be a way out for the policymakers in mapping tree species as well as their probable ecological significance in urban areas over the traditional methods

convenience and suitability of utilizing LiDAR and WV3 image data, especially in the case of vegetation mapping along with their functional attributes. This study could assist future research in either case of tree classification or mapping ecosystem services, having a significant prospect on remote sensing applications in the case of heterogeneous urban areas. Especially for the developing countries or where the application of LiDAR data is not that cost-effective, this mapping approach will show the alters with WV-3 image data. Soon another study will be introduced to compare the CS mapping outcomes between the WV-3 data and the Sentinel 3 data in the case of urban trees.

This study will contribute to a better understanding of the methodology in mapping structural and functional properties, such as tree CS, as well as predicting the possible urban CS in typical city areas. It might be a way out for the policymakers in mapping tree species as well as their probable ecological significance in urban areas over the traditional methods. Thus, the researchers and city planners could go forward to employ and implement the advanced ways of CS mapping for the typical urban areas assessing the possible prospects of the approach against the unavoidable impacts of climate change.

References

146.   Jacobs. *Annual Report*. 2018. Available online: https://www.jacobs.com/sites/default/files/files/2018-12/Jacobs-2018-Annual-Report.pdf (accessed on 24 May 2021).

147.   Jombo, S.; Adam, E.; Byrne, M.J.; Newete, S.W. Evaluating the capability of Worldview-2 imagery for mapping alien tree species in a heterogeneous urban environment. *Cogent Soc. Sci.* **2020**, *6*, 1754146. [CrossRef]

148.   Lumnitz, S.; Devisscher, T.; Mayaud, J.R.; Radic, V.; Coops, N.C.; Griess, V.C. Mapping trees along urban street networks with deep learning and street-level imagery. ISPRS J. *Photogramm. Remote Sens.* **2021**, *175*, 144–157. [CrossRef]

149.   Wang, M.; Liu, R.; Lu, X.; Ren, H.; Chen, M.; Yu, J. The use of mobile lidar data and Gaofen-2 image to classify roadside trees. *Meas. Sci. Technol.* **2020**, *31*, 125005. [CrossRef]

150.   He, S.; Du, H.; Zhou, G.; Li, X.; Mao, F.; Zhu, D.; Xu, Y.; Zhang, M.; Huang, Z.; Liu, H.; et al. Intelligent Mapping of Urban Forests from High-Resolution Remotely Sensed Imagery Using Object-Based U-Net-DenseNet-Coupled Network. *Remote Sens.* **2020**, *12*, 3928. [CrossRef]

151.   Rasti, B.; Ghamisi, P.; Gloaguen, R. Fusion of Multispectral LiDAR and Hyperspectral Imagery. In Proceedings of the IGARSS 2020—2020 IEEE International Geoscience and Remote Sensing Symposium; Institute of Electrical and Electronics Engineers (IEEE), Online, 24 February 2020; pp. 2659–2662.

152.   Zhang, Y.; Shao, Z. Assessing of Urban Vegetation Biomass in Combination with LiDAR and High-resolution Remote Sensing Images. *Int. J. Remote Sens.* **2021**, *42*, 964–985. [CrossRef]

153.   Hansch, R.; Hellwich, O. Fusion of Multispectral LiDAR, Hyperspectral, and RGB Data for Urban Land Cover Classification. *IEEE Geosci. Remote Sens. Lett.* **2021**, *18*, 366–370. [CrossRef]

154.   Li, D.; Ke, Y.; Gong, H.; Li, X. Object-Based Urban Tree Species Classification Using Bi-Temporal WorldView-2 and WorldView-3 Images. *Remote Sens.* **2015**, *7*, 16917–16937. [CrossRef]

155.   Nölke, N. Continuous Urban Tree Cover Mapping from Landsat Imagery in Bengaluru, India. *Forests* **2021**, *12*, 220. [CrossRef]

156.   Mustafa, Y.; Habeeb, H.N.; Stein, A.; Sulaiman, F.Y. Identification and mapping of tree species in urban areas using worldview-2 imagery. *ISPRS Ann. Photogramm. Remote Sens. Spat. Inf. Sci.* **2015**, *II-2/W2*, 175–181. [CrossRef]

157. Fang, F.; McNeil, B.E.; Warner, T.A.; Maxwell, A.E.; Dahle, G.A.; Eutsler, E.; Li, J. Discriminating tree species at different taxonomic levels using multi-temporal WorldView-3 imagery in Washington D.C., USA. *Remote Sens. Environ.* **2020**, *246*, 111811. [CrossRef]

158. Laliberte, A.S.; Koppa, J.; Fredrickson, E.L.; Rango, A. Comparison of Nearest Neighbor and Rule-based Decision Tree Classification in an Object-oriented Environment. In Proceedings of the 2006 IEEE International Symposium on Geoscience and Remote Sensing, Denver, CO, USA, 31 July–4 August 2006; pp. 3923–3926.

159. Le Louarn, M.; Clergeau, P.; Briche, E.; Deschamps-Cottin, M. "Kill Two Birds with One Stone": Urban Tree Species Classification Using Bi-Temporal Pléiades Images to Study Nesting Preferences of an Invasive Bird. *Remote Sens.* **2017**, *9*, 916. [CrossRef]

160. Salih, A.A.; Ganawa, E.-T.; Elmahl, A.A. Spectral mixture analysis (SMA) and change vector analysis (CVA) methods for monitoring and mapping land degradation/ desertification in arid and semiarid areas (Sudan), using Landsat imagery. *Egypt. J. Remote Sens. Space Sci.* **2017**, *20*, S21–S29. [CrossRef]

161. Waser, L.T.; Küchler, M.; Jütte, K.; Stampfer, T. Evaluating the Potential of WorldView-2 Data to Classify Tree Species and Different Levels of Ash Mortality. *Remote Sens.* **2014**, *6*, 4515–4545. [CrossRef]

162. Kumar, L.; Mutanga, O. Remote Sensing of Above-Ground Biomass. *Remote Sens.* **2017**, *9*, 935. [CrossRef]

163. Zhou, W.; Cadenasso, M.L.; Schwarz, K.; Pickett, S.T. Quantifying Spatial Heterogeneity in Urban Landscapes: Integrating Visual Interpretation and Object-Based Classification. *Remote Sens.* **2014**, *6*, 3369–3386. [CrossRef]

164. Cadenasso, M.L.; Pickett, S.T.; McGrath, B.; Marshall, V. *Ecological Heterogeneity in Urban Ecosystems: Reconceptualized Land Cover Models as a Bridge to Urban Design*; Springer Science and Business Media LLC: Cham, Switzerland, 2013; pp. 107–129.

165. Band, L.E. *Heterogeneity in Urban Ecosystems: Patterns and Process, Ecosystem Function in Heterogeneous Landscapes*; Springer: New York, NY, USA, 2005; pp. 257–278.

166. Houghton, R.A.; House, J.I.; Pongratz, J.; Van Der Werf, G.R.; DeFries, R.S.; Hansen, M.C.; Le Quéré, C.; Ramankutty, N. Carbon emissions from land use and land-cover change. *Biogeosciences* **2012**, *9*, 5125–5142. [CrossRef]

167. Oughton, R.A.H. Aboveground Forest Biomass and the Global Carbon Balance. *Glob. Chang. Biol.* **2005**, *11*, 945–958. [CrossRef]

168. Hurtt, G.; Zhao, M.; Sahajpal, R.; Armstrong, A.; Birdsey, R.; Campbell, E.; Dolan, K.A.; Dubayah, R.; Fisk, J.P.; Flanagan, S.; et al. Beyond MRV: High-resolution forest carbon modeling for climate mitigation planning over Maryland, USA. *Environ. Res. Lett.* **2019**, *14*, 045013. [CrossRef]

169. Hurtt, G.C.; Fisk, J.; Thomas, R.Q.; Dubayah, R.; Moorcroft, P.R.; Shugart, H.H. Linking models and data on vegetation structure. *J. Geophys. Res. Space Phys.* 2010, *115*. [CrossRef]

170. Gu, H.; Williams, C.A.; Ghimire, B.; Zhao, F.; Huang, C. High-resolution mapping of time since disturbance and forest carbon flux from remote sensing and inventory data to assess harvest, fire, and beetle disturbance legacies in the Pacific Northwest. *Biogeosciences* **2016**, *13*, 6321–6337. [CrossRef]

171. Huang, W.; Dolan, K.A.; Swatantran, A.; Johnson, K.D.; Tang, H.; O'Neil-Dunne, J.; Dubayah, R.; Hurtt, G. High-resolution mapping of aboveground biomass for forest carbon monitoring system in the Tri-State region of Maryland, Pennsylvania and Delaware, USA. *Environ. Res. Lett.* **2019**, *14*, 095002. [CrossRef]

172. Varhola, A.; Coops, N. Estimation of watershed-level distributed forest structure metrics relevant to hydrologic modeling using LiDAR and Landsat. *J. Hydrol.* **2013**, *487*, 70–86. [CrossRef]

173. Simonson, W.D.; Allen, H.D.; Coomes, D.A. Applications of airborne lidar for the assessment of animal species diversity. *Methods Ecol. Evol.* **2014**, *5*, 719–729. [CrossRef]

174. Goodwin, N.R.; Coops, N.C.; Tooke, T.R.; Christen, A.; Voogt, J. Characterizing urban surface cover and structure with airborne lidar technology. *Can. J. Remote Sens.* **2009**, *35*, 297–309. [CrossRef]

175. Alonzo, M.; Bookhagen, B.; McFadden, J.P.; Sun, A.; Roberts, D.A. Mapping urban forest leaf area index with airborne lidar using penetration metrics and allometry. *Remote Sens. Environ.* **2015**, *162*, 141–153. [CrossRef]

176. Shrestha, R.; Wynne, R.H. Estimating Biophysical Parameters of Individual Trees in an Urban Environment Using Small Footprint Discrete-Return Imaging Lidar. *Remote Sens.* **2012**, *4*, 484–508. [CrossRef]

177. Raciti, S.M.; Hutyra, L.R.; Newell, J.D. Mapping carbon storage in urban trees with multi-source remote sensing data: Relationships between biomass, land use, and demographics in Boston neighborhoods. *Sci. Total. Environ.* **2014**, *500-501*, 72–83.[CrossRef]

178. Jones, T.G.; Coops, N.C.; Sharma, T. Assessing the utility of airborne hyperspectral and LiDAR data for species distribution mapping in the coastal Pacific Northwest, Canada. *Remote Sens. Environ.* **2010**, *114*, 2841–2852. [CrossRef]

179.	Wang, K.; Wang, T.; Liu, X. A review: Individual tree species classification using integrated airborne LiDAR and optical imagery with a focus on the urban environment. *Forests* **2019**, *10*, 1. [CrossRef]

180.	Ørka, H.O.; Hauglin, M. Use of Remote Sensing for Mapping of Non-Native Conifer Species. INA fagapport 33. 76p. 2016. Available online: http://www.umb.no/statisk/ina/publikasjoner/fagrapport/if33.pdf (accessed on 24 May 2021).

181.	Hummel, S.; Hudak, A.T.; Uebler, E.H.; Falkowski, M.J.; Megown, K.A. A Comparison of Accuracy and Cost of LiDAR versus Stand Exam Data for Landscape Management on the Malheur National Forest. *J. For.* **2011**, *109*, 267–273. [CrossRef]

182.	LAND INFO Worldwide Mapping, L. Satellite Imagery Pricing—Satellite Imagery Solutions & Digital Map Data—LAND INFO Worldwide Mapping. Available online: https://landinfo.com/satellite-imagery-pricing/ (accessed on 18 May 2021).

183.	Green Structure and Urban Planning—Final Report. Available online: https://www.cost.eu/publications/green-structure-and-urban-planning-final-report/ (accessed on 17 August 2020).

184.	Sturiale, L.; Scuderi, A. The Role of Green Infrastructures in Urban Planning for Climate Change Adaptation. *Climate* **2019**, *7*, 119.[CrossRef]

The paper originally published in Forests 2021, 12,692. https://doi.org/10.3390/ f12060692 has been republished wth authors' permission. ◣

NASA, Partners develop 'Lunar Backpack' technology

Imagine a mountaineering expedition in a wholly uncharted environment, where the hikers had the ability to generate a real-time 3D map of the terrain. NASA researchers and their industry partners have developed a remote-sensing mapping system set to aid explorers in the most isolated wilderness imaginable: the airless wastes at the South Pole of the Moon.

Credits: NASA/Michael Zanetti

The Kinematic Navigation and Cartography Knapsack (KNaCK) is a mobile lidar scanner – a remote sensing method that uses light detection and ranging laser light to measure range. Donned like a hiker's backpack, it makes use of an innovative type of lidar called frequency modulated continuous wave (FMCW) lidar in order to provide Doppler velocity and range for millions of measurement points per second. These measurement points instantly create a real-time navigation system, delivering to the explorer a 3D "point cloud" or high-resolution map of the surrounding terrain.

Think of it as a superpowered version of laser range finders used by surveyors or the highly sensitive proximity alarms that help smart cars avoid collisions, said planetary scientist Dr. Michael Zanetti, who leads the KNaCK project at NASA's Marshall Space Flight Center in Huntsville, Alabama.

"Basically, the sensor is a surveying tool for both navigation and science mapping, able to create ultra-high-resolution 3D maps at centimeter-level precision and give them a rich scientific context," Zanetti said. "It also will help ensure the safety of astronauts and rover vehicles in a GPS-denied environment such as the Moon, identifying actual distances to far-off landmarks and showing explorers in real time how far they've come and how far is left to go to reach their destination."

That's a key challenge as Artemis-era explorers prepare to undertake the first modern missions to the Moon, and the first ever to its South Pole. The Sun never rises more than 3 degrees above the lunar horizon there, leaving much of the terrain in deep shadow. That makes distances to various points of interest difficult to eyeball.

Initiated in 2020 with funding by NASA's Early Career Initiative, the KNaCK project has partnered with Torch Technologies Inc. of Huntsville to develop the backpack prototype and associated navigation algorithms that permit accurate mapping without GPS.

Using KNaCK during rover excursions and when traveling on foot, explorers could precisely map the topography of the landscape, including deep ravines, mountains, and caves. Lidar even works in pitch blackness, relieving astronauts of the need to haul cumbersome lighting rigs everywhere they go.

Next, the KNaCK team will work to miniaturize the hardware – the backpack prototype weighs about 40 pounds – and harden the sensitive electronics against the punishing effects of microgravity and solar radiation.

Molly Porter
Marshall Space Flight Center, Huntsville, Alabama
nasa.gov ◣

Is India's forest cover really increasing? Official maps don't tell you the whole truth

No, India's forest cover has not increased steadily. Instead, tea estates, coconut plantations, and even tree-lined avenues are being classified as forests

M D Madhusudan
Ecologists.

T R Shankar Raman
Ecologists.

It is not long after dawn, but the air in the Borajan rainforest in upper Assam is already warm and heavy with humidity. On a fig tree by the dirt track cutting through the forest, a pair of oriental pied hornbills hop heavily from branch to branch, searching for ripe fruit. From the boughs above them comes the be-quick call of a fairy bluebird. Then, the chorus begins.

What starts as a couple of hesitant, mellow coos, erupts into an exuberant crescendo of shrill, rising hoots, shrieks and yowls. The arboreal orchestra reverberates through the forest for a full 20 minutes. Yet, these powerful vocalists — a family of hoolock gibbons, India's only ape and a gravely endangered primate — are surprisingly bashful and hard to sight. When they finally reveal themselves, the chorus is over, and the family is perched quietly on a shamkathal tree. With one hand on her clinging infant, another holding on to a branch above, the brown-furred mother sits still, with an almost wistful look in her eyes, as she gazes into the distance.

If you follow her gaze, you'd see the forest canopy thin out rapidly, and the undergrowth become a thick, disorderly tumble for a 100 or so metres, then open out into a vast, manicured area of waist-high tea bushes. It is a green expanse, with a tree here and there, but neither the scattered trees nor the tea is gibbon territory. Her performing stage, the home of her family — and indeed, her entire world — is in the dense canopy of rainforest trees, strung with lianas, full of flowers buzzing with myriad insects, and laden with fruit over which birds, squirrels, and monkeys squabble. And that world ends with the forest where she sits, beyond which an unliveable green expanse opens out.

Over time, the definition of 'forest' has been changed to include tea estates like this one, coconut plantations and more. | Photo Credit: Getty Images/iStockphoto

A hoolock gibbon with its baby at Assam zoo

Going extinct

In 15 years, the Borajan rainforest patch has lost over two-thirds of its gibbons. The remaining gibbons that can neither live in nor move through the surrounding tea plantations are isolated. In the nearby forests of Bherjan and Podumoni, which together make up a sanctuary, the gibbon has already gone extinct. Other primates, such as macaques and capped langurs, too have declined or disappeared.

Had the mother gibbon in Borajan not been reading her landscape as every gibbon learns to do, but instead consulted India's official maps of forest cover, she would have discovered that, according to the authorities, her forest, in fact, did not end at all. It stretched beyond the rainforest, well into the tea. Even as India's official reports have been claiming every two years that the country's forest cover is going up and up, the same reports have also been lumping natural forests and commercial plantations as 'forest', a decision defended recently even by the environment Minister.

To understand the sleight of hand, one needs to understand how forest cover is being defined and recorded, and why, if not done right, headlines claiming 'forest cover up' may, in reality, imply a forest cover-up.***

Since 1987, the Forest Survey of India has put out India State of Forest Reports (ISFRs) every two years. The broad intent of these reports has been to track the wealth and health of our forests. In its first decade, the ISFRs reported a decline of some 7,400 sq.km. Thereafter, the forest cover of India, as reported in the ISFRs, has increased by an eye-popping 80,000 sq.km. Yet, for ecologists in the field, and for communities on the ground, this official narrative of steadily increasing forest cover has been remarkably hard to validate. So, what is actually going on?

Starting in 2001, the ISFRs made some big changes to the way they classified

and counted pixels in a satellite image as forest. They began using finer-scaled satellite imagery and an entirely digital workflow to analyse them. In addition, the ISFRs also changed their definition of a forest. They now explicitly included any lands of at least one hectare area and with 10% or more tree cover, regardless of the tree species on the land, or the purpose for which it was grown, or its ownership, as forest. So, all of a sudden, tea estates, coconut plantations, mango orchards, homestead gardens of suburban housing developments, and even tree-lined avenues in densely built-up cities were being classified as 'forest'. In one stroke, just between the 1999 and the 2001, this redefinition helped raise India's forest cover by over 38,000 sq.km., the size of Kerala.

What a map of the Borajan forest will actually look like today to the hoolock gibbon, its inhabitant

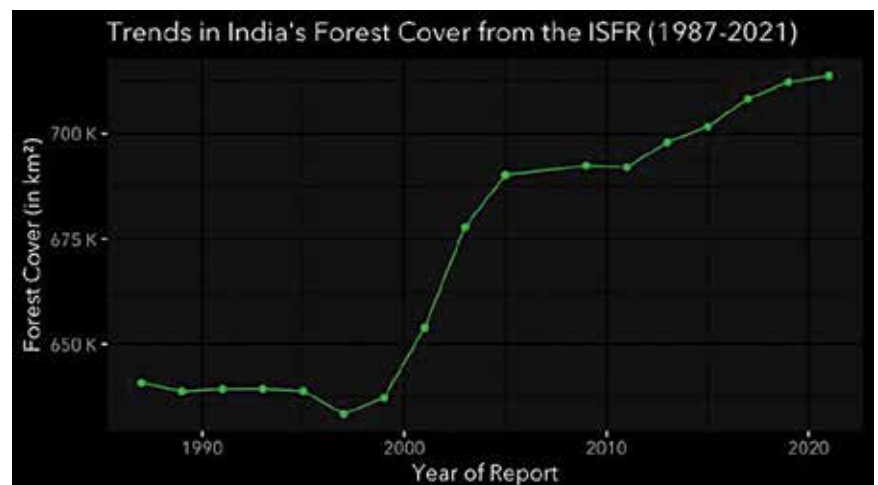**Plotting ISFR figures of India's forest cover growth over 30 years**

Gardens and boulevards

To be clear, there is no harm in mapping and counting tree-covered areas such as plantations, estates, orchards, farms, gardens, and boulevards created through human activity. But what is pernicious is that the ISFRs lump them into the same category as natural forests, whose ecological, economic, and cultural values are incomparably greater and more diverse. Converting any natural habitat into a human-managed land-use area has huge consequences for the land, the kinds of livelihoods it can sustain, and for the lifeforms that can survive in it. ***

Scientific studies have shown that monocultures, such as of eucalyptus or acacia wattles, have a pronounced

hydrological impact. Compared to forests or other natural vegetation such as grasslands, such plantations deplete groundwater, have higher surface water runoff, poorer infiltration, and allow only shorter duration dry season flows in nearby streams. Recent studies from the Nilgiris by researchers from ATREE, Bengaluru, and FERAL, Pondicherry, also indicate that plantations can expose catchments to higher risk of floods during extreme rainfall events.

Plantations are also poorer than forests in carbon sequestration, a key ecosystem function essential to tackling the climate crisis. In the Western Ghats, scientists report that carbon stocks in plantations such as teak and eucalyptus are 30% to 50% lower than in natural evergreen forests. Even where carbon stocks in plantations match some forests such as deciduous forests, they are still less stable and resilient than those of natural forests, especially in drought years. India's ambitious goals under the Bonn Convention and UNFCCC to absorb 2.5 to 3 billion tonnes of carbon dioxide from the atmosphere would be far better served by protection and restoration of natural forests than through tree plantations.

Natural produce

Natural forests are also important livelihood and cultural spaces for millions of forest-dependent people. Tree plantations, in contrast, tend to erode such cultures and livelihoods. In central and eastern India, tribal communities dependent on a wide range of produce from natural forests (such as tendu leaves, mahua flowers, fruits, firewood, and medicines) have had their access to these resources curtailed or denied when the areas were converted to 'compensatory afforestation' plantations. A teak plantation is simply no match for a diverse natural forest in the range of resources it provides local people.

The loss and fragmentation of natural forests can also lead to severe economic losses and elevate public health risks.

A coconut grove in Tamil Nadu.

Extensive deforestation in Sonitpur, Assam between 1997 and 2005 led to huge increases in crop losses, deaths of both elephants and humans in conflicts, and an eight-fold increase in malaria in the deforested regions. Mapping such landscape transformation accurately is vital for conservation planning. But sadly, this is easily overlooked when we make poor maps of forest cover that do not distinguish natural forests from highly-modified landscapes merely because the latter meet ISFR's minimum criteria of 10% tree cover across a hectare to qualify as a 'forest'.

A third aspect, one that the Borajan gibbons know with every fibre of their being, is amply evidenced by research from around the world. For biodiversity, especially for endemic and forest-dependent species such as gibbons, plantations support far fewer species than forests. Studies from many parts of India have shown that monoculture plantations of various kinds — oil palm, teak, eucalyptus, pine, and others — have fewer plant and animal species compared to the natural forests in their respective regions. In Mizoram, for instance, oil palm plantations have only about one-seventh the number of bird species compared to the natural evergreen forests here. Most of the species that manage to survive in plantations are plants and animals of disturbed, open habitats — such as

The oriental pied hornbill

common tailorbirds — that replace native species that include many rare ones and endemics, such as understorey flycatchers and trogons. Similar differences exist between forests and other human-modified tree-covered habitats such as urban parks, campuses, and home-gardens.

Mapping changes

It is not that plantations or urban parks do not have any value for biodiversity. Tea plantations may never be able to support species like gibbons, because the habitat is too altered and the resources such as fruits that the gibbons need are simply

not there. But some plantations, such as coffee plantations established under native shade trees in the Western Ghats, may support animals including lion-tailed macaques, an endemic and endangered primate, when such plantations adjoin the wet evergreen forests that are the natural habitat of the species. Forest birds including minivets and tree-dwellers such as giant squirrels may also survive in such plantations, but at lower numbers and only when they adjoin natural forests. Agro-forestry plantations may serve as a kind of buffer habitat in the countryside landscape just as urban parks provide welcome greenery in a city, but neither can become a replacement for natural forests.

So, for all these reasons, if India's overall increase in forest cover is due to an increase in plantations, while natural forests are declining, it will have serious negative impacts on ecology and economy, climate and biodiversity. This is why it is essential to tease them apart and map changes in plantations and natural forests separately. ***

An oil palm plantation in Andhra Pradesh

A tea garden in Sonitpur, Assam

Going forward, it is vital that we understand the huge differences between natural forests and other tree-covered landscapes created by humans. The FAO's Global Forest Resources Assessment 2020 reports that since 1990, India's naturally regenerating forests increased only marginally by 6,700 sq.km. while, over the same period, plantations increased by 75,500 sq.km. About 92% of India's so-called 'forest cover increase' between 1990 and 2020 has thus been via plantations.

It is critical that the ISFRs start tracking the well-being of our natural forests separately from other 'green' areas that humans are continuing to create by destroying natural habitats. Failing to do so means that we could be presiding over the loss of our natural forests and hastening the impact of climate change even as we mistakenly cheer the increase in various forms of commercial tree cover as gains in forest cover.

Natural forests are not merely the volume and variety of trees they contain. They are an entire magical world unto themselves, a vast web of complex relationships between countless lifeforms, holding incomparably greater ecological value and offering vastly greater economic and cultural benefits than the densest plantation, the most bounteous orchard, or the prettiest tree-lined boulevard.

But what we choose to call a forest must also make sense to that mother gibbon in Borajan, swinging and singing in her rainforest canopy, and to countless other creatures like her for whom the forest is home.

The article originally published in The Hindu is republished with permission.

First high–orbit GLONASS satellite in 2028

Russia plans to launch the first of the six high-orbit GLONASS satellites into orbit in 2028, according to the head of the GLONASS Application Division in the Russian space agency Roscosmos, Ivan Revnivykh. Such satellites will be able to transmit two navigational signals with code division in the L1 and L2 frequency bands and improve the accuracy and accessibility of services in complex conditions, in particular, in the Arctic. *https://tass.com/science*

Protecting third–party timing receivers from cyber attacks

ADVA has extended its Ensemble Sync Director GNSS assurance software to integrate any third-party vendor's GNSS receiver observables at scale. A key pillar of ADVA's Ensemble Sync Director can now transparently show and analyze GNSS observables from third-party receivers in even the largest deployments. This is key as synchronization based on satellite signals is vulnerable to failure, interference and cyberthreats, and so network operators urgently need to protect their critical timing with continuous monitoring and assurance. Now, they have the power to remotely detect issues with GNSS receivers from any vendor, helping to maintain high-quality timing performance, avoid disruptions and reduce operating costs. *www.adva.com*

i83 IMU–RTK GNSS receiver by CHC navigation

CHC Navigation has announced the availability of the i83 GNSS receiver, an addition to its premium GNSS receiver series for surveying, mapping and construction professionals. It is powered by a 1408-channel multi-band GNSS receiver, the latest iStar technology, and a calibration-free, high-end inertial measurement unit (IMU) for faster and reliable field GNSS surveying. The third-generation high-gain antenna with the latest advanced CHCNAV iStar algorithm improves GNSS satellite signal tracking efficiency by more than 30%. *www.chcnav.com*

Flight trials by AAI using GAGAN based LPV approach procedure

Airports Authority of India (AAI) has successfully conducted at Kishangarh Airport, Rajasthan light trial using GAGAN (GPS Aided GEO Augmented Navigation) based LPV Approach Procedures. The successful trial is a great achievement and major milestone in field of Air Navigation Services (ANS) in the history of Indian Civil Aviation Sector. India is the first country in Asia Pacific Region to achieve such a landmark.

LPV (Localizer Performance with Vertical Guidance) permits aircraft guided approaches that are operationally nearly equivalent to Cat-IILS, without the need for ground-based navigational infrastructure. The service relies on the availability of GPS and GAGAN Geo Stationary Satellites (GSAT-8, GSAT-10 and GSAT-15), launched by ISRO.

GAGAN is an Indian Satellite Based Augmentation System (SBAS) jointly developed by AAI and ISRO. It is the first such system developed for India and neighboring countries in the equatorial region. GAGAN System was certified by DGCA in 2015 for Approach with Vertical Guidance (APV 1) and en-route (RNP 0.1) operations. There are only four Space-Based augmentation systems available in the world namely India (GAGAN), US(WAAS) Europe (EGNOS) and Japan (MSAS).

Indigo Airlines using its ATR aircraft has flown an Instrument Approach Procedure (IAP) with LPV minima of 250ft, using GAGAN Service. The tests at Kishangarh Airport were performed as part of initial GAGAN LPV flight trials along with DGCA team on- board. After the final approval by DGCA, the procedure will be available for usage of commercial flights.

LPV is a Satellite Based Procedure which has been used by the aircraft for landing purpose at Kishangarh Airport (Rajasthan). LPV approaches will make it possible to land at airports not equipped with expensive Instrument Landing Systems, which includes many small regional and local airports. Lowering the decision height up to 250 ft provides a substantial operational benefit in poor weather and low visibility conditions. Thus, any airport which hitherto would require higher visibility minima, will be able to accept aircraft benefitting remote airports which are devoid of precision approach capability equipment.

Number of airports including airports under Regional Connectivity Scheme (RCS) are being surveyed for development of GAGAN based LPV Instrument Approach Procedures so that suitably equipped aircraft can derive maximum benefit in terms of improved safety during landing, reduction in fuel consumption, reduction in delays, diversions and cancellations etc.

Design of GAGAN procedures require meticulous survey of the airport environment surroundings and obstacle surfaces. These data are correlated with the complex aircraft approach maneuvers and further simulated in a software to ensure safety of the procedure designed. These procedures can be developed for any of the airport in India for landing without help of Instrument Landing System.These types of procedures make aircraft to land in low visibility condition almost equivalent to Category-1 Instrument Landing System (ILS). Currently Indigo (35), SpiceJet (21), Air India (15), Go First (04), Air Asia (01) and other airlineshave aircraft in their fleet capable to use these LPV procedures. Airports Authority of India has developed 22 such procedures and some are under process of approval from DGCA for commercial flight operations. In line with Govt. of India initiative of AtamNirbhar Bharat, development of LPV procedures for all civil airports is also in progress to make Indian civil aviation sector more self-reliant. *www.aai.aero*

PAR Government rebrands situational awareness solution

PAR Government, a provider of geospatial and decision support solutions for 57 years, has rebranded its TeamConnect™ cloud-based situational awareness suite as Sit(x)™. The commercial Sit(x) solution is designed for enhanced collaboration among government and civilian public safety organizations. PAR Government Systems Corporation (PGSC) is a wholly owned subsidiary of PAR Technology Corporation. *www.pargovernment.com*

BISim launches Mantle ETM

Bohemia Interactive Simulations (BISim) has launched its new technology product, Mantle Enterprise Terrain Management (ETM), which is a custom-built platform based on proven COTS components and expert design/development services for creating simulated terrain for training, mission rehearsal, visualization and terrain analysis. *https://bisimulations.com*

Kraken completes RaaS contract from Government of Canada

Kraken Robotics Inc. has successfully completed a Robotics as a Service (RaaS) contract with the Royal Canadian Navy (RCN), for testing of Kraken's ultra-high resolution survey equipment. This $0.5 million contract was funded under the government of Canada's Innovative Solutions Canada program, and the testing department for this service offering was the RCN's Fleet Diving Unit Atlantic (FDU-A) based in Halifax, Nova Scotia. The RCN has a mandate to develop and maintain an advanced sonar imaging and data storage capability

for all three coasts, and to deploy this capability to national and international areas of interest. This contract provided the RCN FDU-A access to cutting edge technology and high-resolution seabed data. *www.krakenrobotics.com*

Showing new light for global warming challenge

A group of scientists have computationally designed a hybrid material, which can absorb greenhouse gas methane, converting it to clean Hydrogen and also simulated a process of capturing carbon dioxide in-situ and converting it to high purity hydrogen from non-fuel grade bioethanol. They have also designed a facility that can test such materials and help further carbon capture research at the institute.

Given the global warming potential of greenhouse gases, scientists are trying to explore innovative methods of absorbing these gases and converting them to useful substances. New materials that can play dual role of absorption as well as conversion is the new challenge area for scientist in carbon capture innovation.

Responding to the challenge, in a series of researches on carbon capture and utilization scientists from Indian Institute of Chemical Technology (IICT), Hyderabad have not only computationally designed a hybrid material that can capture methane and also act as catalyst to convert it to high purity hydrogen, but also simulated and designed a process for in situ capture of carbon dioxide and its conversion to high purity hydrogen from non-fuel grade bioethanol through a mechanism called the optimized intensified chemical looping reforming. *https://dst.gov.in* ⊾

"The monthly magazine on Positioning, Navigation and Beyond"
Download your copy of Coordinates at
www.mycoordinates.org

Advance autonomous vehicle scaled production program

Perrone Robotics, Inc. and Roush Industries has completed the first phase of a successful TONY® - AV, fully autonomous, zero-emissions, electric shuttle integration. The new prototype will be the model for a large-volume production process that will allow Perrone's TONY AV-Retrofit kit to be easily integrated into existing vehicle models at scale. *www.perronerobotics.com*

Isuzu Australia drives forward with HERE

Isuzu Trucks has deployed HERE Navigation, an off-the-shelf navigation solution for embedded in-vehicle infotainment (IVI) platforms, in its new 2022 model year F Series, FX Series and FY Series trucks sold in Australia. HERE Navigation optimizes Isuzu's fleet operations with a connected in-vehicle navigation system. *www.here.com*

Baidu wins first driverless permits in China

Baidu, Inc. has received the first-ever permits in China authorizing the company to provide driverless ride-hailing services to the public on open roads in Beijing. This regulatory approval marks a significant milestone for the autonomous ride-hailing industry in China, indicating a regulatory openness to taking a further step toward a fully driverless mobility future.

With these permits issued by the head office of the Beijing High-level Automated Driving Demonstration Area (BJHAD), ten autonomous vehicles without drivers behind the steering wheel will offer rides to passengers in a designated area of 60 square kilometers in Beijing. These licensed cars will join an existing fleet provided by Apollo Go, Baidu's autonomous ride-hailing service, in the capital city of China. Starting April 28, 2022, users were able to hail a driverless ride using the Apollo Go mobile app in daytime. *baidu.com*
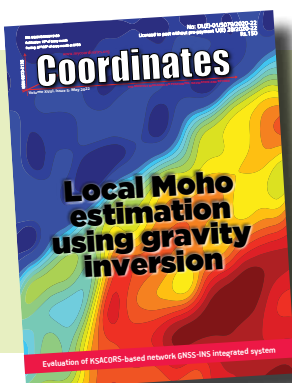
Driver–assistance technology for collision avoidance

Nissan has announced a new driver-assistance technology, which is currently in-development that utilizes highly accurate, real-time information about the vehicle's surrounding environment to dramatically enhance collision avoidance.

Nissan's "ground truth perception" technology fuses information from next-generation high-performance LIDAR, radar and cameras. The technology can detect the shape and distance of objects, as well as the structure of the area surrounding the vehicle, in real time with a high degree of accuracy. Utilizing this information, it is possible for the vehicle to instantly analyze the current situation, judge and automatically perform required collision-avoidance operations. This technology can also detect slowed traffic and road obstacles in the distance and execute lane changes accordingly. Importantly, the technology can also provide increased support to drivers in areas where detailed map information is not available. *www.nissan-global.com*

Pony.ai to launch fleet of Robotaxis

Pony.ai, global autonomous driving technology company, has announced a deeper partnership with Ontime, GAC's ride-hailing app. As part of the partnership, Pony.ai will integrate its virtual driver technology into GAC vehicles, which will then be used on GAC's Ontime ride-hailing platform. Ontime expects to launch its fee-charging robotaxi service in Guangzhou during 2022. *https://pony.ai*

DeepRoute.ai unveils advanced Robotaxi fleet

DeepRoute.ai, an international autonomous driving technology company, announces a leading-edge Robotaxi fleet equipped with its distinctive L4 autonomous driving solution, Driver 2.0. Composed of 30 SAIC Motor MARVEL R SUVs, the Robotaxi fleet will deploy in Shenzhen, China, in the coming months.

Nearmap and DroneShield join forces

DroneShield Limited has announced an enhanced version of its DroneSentry-C2TMCommand-and-Control software, in partnership with location intelligence firm, Nearmap. It provides an intuitive and feature-rich software platform, providing counter-UAS awareness and reporting capability. It integrates both DroneShield and third-party C-UAS sensors and effectors. Those include multiple AI-enabled sensing and tracking products, such as RfOneTM long-range direction-finding sensors for UAS detection and tracking, and camera-agnostic DroneOptIDTM optical/thermal camera AI software. *www.droneshield.com*

World's largest autonomous commercial drone deployment

Percepto has announced it will deploy autonomous drones to monitor Florida Power & Light's substations and power distribution grids across the state. The first electric utility to deploy drone-in-a-box (DIB) technology statewide, the arrangement represents the largest commercial autonomous drone project in the world. It's also the first operation using autonomous drones within an urban setting for infrastructure inspection to ensure quality service to FPL customers. *www.percepto.co*

Interim approval to 'Kisan Drones' in India

More than two months after it was announced in the Union Budget, the government recently granted an interim approval for spraying of nearly all the registered pesticides formulations using Kisan Drones and also brought out the standard operating procedures (SOPs).

Kisan Drones are slated to be used in pesticide and nutrient application by providing precise instructions for effective and safe operations of drones. The Department of Agriculture and Farmers` Welfare has brought out the SOPs after consultation with the stakeholders on this sector. *www.dnaindia.com*

Pixxel launches first commercial satellite

Pixxel, the Indian Space-tech startup has launched its first commercial satellite, TD-2. It is a full-fledged commercial satellite that hosts one of the highest resolution hyperspectral commercial cameras to be ever flown. It has been launched with SpaceX's Falcon-9 rocket, in order to build a 24×7 health monitor for the planet. With more satellites scheduled to launch in late 2023, Pixxel aims to achieve daily global coverage by early 2024. *www.pixxel.space*

UK Space Command Contracts with SSTL

Surrey Satellite Technology Ltd (SSTL) has signed an £22m contract with Defense Equipment and Support on behalf of Space Command for Carbonite+, a 150kg spacecraft. Project TYCHE is the first satellite procurement for the MINERVA programme which is a key enabler in the development of the foundation for a UK Space-based Intelligence Surveillance & Reconnaissance (ISR) constellation under programme ISTARI. Delivered under a 3 year build programme, the Carbonite+ mission will be compatible with both horizontal as well as vertical launch. Carbonite+ will be operated from SSTL's Spacecraft Operations Centre in Guildford. *www.sstl.co.uk*

New technology for mapping and analyzing space debris by Fujitsu

Fujitsu has announced the development and deployment of a new analysis system to calculate orbital courses of space debris for use with the Japan Aerospace Exploration Agency's (JAXA) "Space Situational Awareness System" ("SSA system") for monitoring space debris. JAXA started operations of the new system at the Tsukuba Space Center on April 1, 2022. JAXA will utilize the new technology to create plans on effective space debris observation, drawing on observation data from radar and optical telescope to calculate the trajectory of space debris and perform comparative analysis with the path of JAXA satellites.

In case the system detects space debris approaching satellites, it will support the operators at JAXA in quickly responding to risks and avoid any possible collisions with the space debris by automatically calculating the possibility of a predicted collision and necessary course changes. *www.fujitsu.com*

Space industry launches humanitarian initiative to support Ukraine

Leaders of the space community have announced the Space Industry for Ukraine (SIFU), an initiative designed to fund and execute efforts that provide immediate humanitarian aid to the people of Ukraine. The initiative will be run by a steering committee, which includes HawkEye 360, National Security Space Association (NSSA), ABL Space Systems, ARKA, BlackSky, Capella Space, ICEYE, Insight Partners, Leidos, LeoLabs, Maxar, Raytheon Intelligence & Space, Rebellion Defense, Relativity Space, Riverside Research, Rocket Lab, Velos and Viasat. The steering committee will fundraise, select and monitor the execution of critical humanitarian projects throughout Ukraine and its neighboring countries. Additional participating donor companies include The Aerospace Corporation, Cognitive Space and Shield Capital. Through the generous contributions of its members, the SIFU has fundraised to date nearly $1 million. In coordination with the international NGO community and with representatives of the Polish and Ukrainian governments, high-value projects have been structured to be undertaken on short notice to create immediate and material value for the Ukrainian cause.

National Space Policy Secretariat of the Cabinet Office contract with Synspective

Synspective Inc., a SAR satellite data and solutions provider, announced that it has entered into a contract for a "demonstration project for expanding the use of small SAR satellite constellations" led by the National Space Policy Secretariat of the Cabinet Office in Japan.

In order to expand the full-scale use of SAR data in domestic ministries and agencies, the National Space Policy Secretariat of the Cabinet Office will lead a project to test small SAR satellite constellations in various administrative fields, and organize and evaluate their effectiveness, feasibility, and issues at an early stage. Furthermore, the project will conduct usage verification in the administrative field for potential usage needs, verify and evaluate effectiveness and feasibility, and sort out any issues that need improvement. Based on the results, the best approaches will be identified for full-scale use in each ministry of the Japanese government to promote future use expansion. *https://synspective.com*

Planet forms strategic relationship with Moody's

Planet has entered into an agreement with Moody's, a leading global integrated risk assessment firm serving financial markets, to explore and address the growing demand for assessing and monitoring solutions on Environmental, Social, and Governance (ESG) risks. This relationship with a global financial firm is a landmark deal for Planet, leveraging satellite data for ESG measurement. As companies and governments face unprecedented risks due to climate change and political upheaval, new and holistic reporting metrics to evaluate the long-term risks and sustainable opportunities of this century are critical to providing information for investors, regulators, and the public. *www.planet.com*

3D LiDAR and deep vision data platforms integration

Quanergy Systems, Inc., provider of LiDAR sensors and smart 3D solutions, has announced a technology integration with Mirasys, one of the leading suppliers of open platform Video Management Systems (VMS). The integration of Quanergy's platform with Mirasys' deep vision data platform will deliver advanced insights and analytics for physical security applications in the government, retail, and gaming industries. *www.quanergy.com*

RIT Digital Imaging and Remote Sensing Lab teams with Rendered.ai

Rendered.ai and the Rochester Institute of Technology's Digital Imaging and Remote Sensing (DIRS) Laboratory announced a collaboration to combine the physics-driven accuracy of the DIRSIG synthetic imagery model with Rendered.ai's cloud-based platform for high volume synthetic data generation.

Machine Learning (ML) algorithms using Computer Vision (CV) data provide a key tool for exploiting the rapidly expanding capability and content of Earth Observations (EO) collection and analytics companies around the world. Rendered.ai provides a platform as a service (PaaS) for data scientists and CV engineers to scalably produce large, configurable synthetic CV datasets in the cloud for training Artificial Intelligence (AI) and ML systems. The DIRSIG model produces a range of simulated output representing passive single-band, multi-spectral, or hyper-spectral imagery from the visible through the thermal infrared region of the electromagnetic spectrum. It is widely used to test algorithms and to train analysts on simulated standard imagery products. *www.rit.edu*

China launches remote sensing on crops

Chinese meteorologists launched monitoring and assessment services for winter wheat distribution across the country that is based on remote sensing satellite technology. The monitoring accuracy reached a resolution of 30 meters from space, and meteorology departments at the national, provincial, municipal and county levels have joined forces to promote such satellite technology applications. The new satellite-powered service could address the previous lack-of-precision problems in weather forecasts for grain production, Zhang Mingwei, an associate research fellow with the National Satellite Meteorological Center who is in charge of the project, told the Global Times on Tuesday. *www.globaltimes.cn*

New Airborne LiDAR Series by CHC navigation

CHC Navigation have recently released the AlphaAir 140 and AlphaAir 2400 LiDAR systems. Both are very lightweight and compact airborne laser scanners that are easily installed on various UAV platforms or small survey aircraft and helicopters. They are ideally adapted to high-density point corridor mapping applications, day or night, under leaf-on and leaf-off conditions or with dense vegetation to provide reliable results.

Septentrio GNSS receivers to support the CLAS

Septentrio has launched three new products: mosaic-CLAS, AsteRx-m3 CLAS and AsteRx SB3 CLAS, which support Japan's high-accuracy Centimeter Level Augmentation Service (CLAS). These multi-frequency GNSS receivers support CLAS on a single device, thanks to the latest GNSS technology which receives the L6 signal, which transmits high-accuracy corrections from Japan's QZSS constellation. *www.septentrio.com*

Hexagon helps electricity Company of Ghana

Hexagon's Safety, Infrastructure & Geospatial division announced the successful deployment of an advanced utility geographic enterprise asset management system (EAM) for the Electricity Company of Ghana (ECG). This smart EAM, featuring Hexagon's G/Technology, will allow ECG to plan, manage and efficiently operate its distribution network to meet the growing needs of 4.5 million customers.

The enterprise system from Hexagon unifies data from a variety of GIS, enabling bi-directional data flow with other systems based on Common Information Model (CIM) standard. The system enhances ECG's ability to geographically reference and manage assets with integrated tools for data surveying, capture and maintenance and network planning and calculation. Mobile capabilities enable efficient inspections and maintenance, while a web portal assists employees with locating assets, reviewing the network and more.

Tallysman wireless adds XF feature to precision GNSS antennas

Tallysman recently added eXtended Filtering (XF) to its line of VeroStar® housed and embedded precision GNSS antennas. The XF feature is designed to mitigate interference from all near-band signals. The antennas provide low elevation angle tracking of the full GNSS spectrum and L-band correction signals. The wideband spherical antenna element enables the antennas to offer ±2 mm phase centre variation (PCV), making them well suited for high-precision marine, positioning and machine control applications.

New Geode GNS3 GNSS Receiver by Juniper Systems

Juniper Systems has introduced the all-new Geode GNS3 GNSS Receiver. It allows users to easily collect real-time GNSS data with sub-meter, sub-foot, and decimeter accuracy options – without the huge price tag or complexity of other precision receivers. This scalable platform allows users to purchase the level of accuracy they need now while having the option to increase accuracy in the future. *www.junipersys.com*

Tracking one million vehicles by 2025

One Step GPS has announced a new target of equipping 1 million vehicles with their GPS technology by 2025. The announcement comes just after receiving a place on the 2022 Inc 5000 Regionals Pacific list on March 15th. One Step GPS is channeling greater resources to become the first-choice GPS tracking software provider on the market, with keen focus on customer support. One Step GPS specializes in software that provides real-time, live tracking features for vehicles. *www.onestepgps.com*

Trimble and Infotech expand collaboration

Trimble and Infotech have an enhanced collaboration to improve the inspection process for civil infrastructure projects. Through the connection of Trimble Access field software and Infotech's Appia service, the software integration streamlines the workflow from survey to construction to provide high-accuracy measurement workflows for daily work reports and inspection reporting for inspectors in engineering, construction and local public agencies. *www.trimble.com*

Hexagon acquires Innovatia Accelerator

Hexagon AB announced the acquisition of Innovatia Accelerator Inc., a developer of SaaS-based digitalization solutions that transform operations and modernize fieldwork in the manufacturing and process industries.

Innovatia Accelerator's flagship solution, AcceleratorKMS, is an AI-based infield knowledge management platform that expedites the digital transformation of paper-based, high-risk operational procedures and work processes. It enables organizations to easily manage, govern and distribute the up-to-date critical operational content field workers require to keep operations running optimally and smoothly. *www.hexagon.com*

GatesAir to introduces timing and signal reference generator

GatesAir's new timing and signal reference solution for broadcast and telecom facilities that speaks to modern navigation technologies used in second-generation GNSS. Its innovation, the Maxiva GNSS-PTP is a standalone 1RU solution with a sophisticated switching algorithm that assures high-precision 10MHz and 1 PPS reference signals to mission-critical components in the signal chain, including transmitters, networking, and studio equipment. Each GNSS-PTP

⌐ MARK YOUR CALENDAR

June 2022

ISPRS Congress 2022
6-11 June
Nice, France
www.isprs2020-nice.com

**8th International Conference
on Cartography and GIS**
20 to 25 June 2022
Nessebar, Bulgaria
https://iccgis2020.cartography-gis.com

July 2022

IGARSS 2022 (hybrid form)
17-22 July 2022
Kuala Lumpur, Malaysia
https://igarss2022.org

August 2022

GeoCart'2022
24 - 26 Aug
Wellington, New Zealand
www.cartography.org.nz

September 2022

**15th Conference on Spatial
Information Theory (COSIT)**
5-9 Sep 2022
Kobe, Japan
cosit2022.iniad.org

Commercial UAV Expo Americas
6-8 September 2022
Las Vegas, USA
www.expouav.com

**17th Symposium on Location
Based Services (LBS2022)**
12-14 Sep 2022
Munich, Germany
lbsconference.org

**18th International Conference on
Geoinformation and Cartography**
14-16 Sep 2022
Zagreb, Croatia
www.kartografija.hr

EuroCarto 2022
19-21 Sep
Vienna, Austria
www.eurocarto2022.org

ION GNSS+ 2022
19-23 September
Denver, CO, USA
www.ion.org/gnss/index.cfm

October 2022

Intergeo Hybrid
18-20 October 2022
Essen, Germany
www.intergeo.de

November 2022

Trimble Dimensions+
7-9 November 2022
Las Vegas, USA
https://dimensions.trimble.com

device feeds up to twelve 10 MHz and 1 PPS references in the technology infrastructure, removing the need to integrate a standalone timing source in each component. This substantially reduces equipment costs and installation timelines while providing a single, yet highly redundant, point of failure for engineers. *www.gatesair.com*
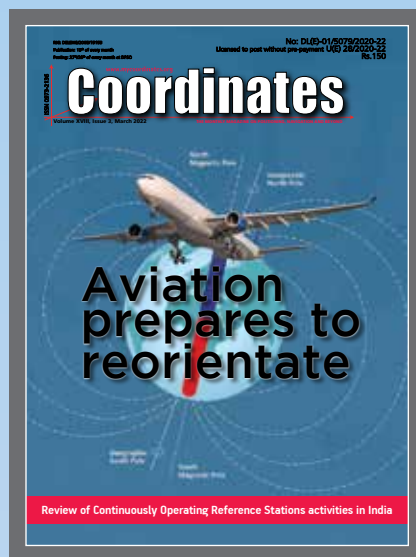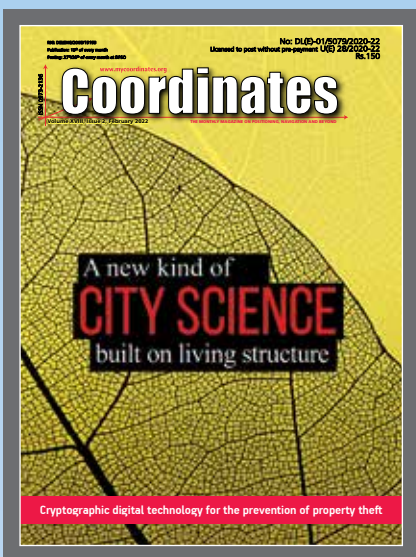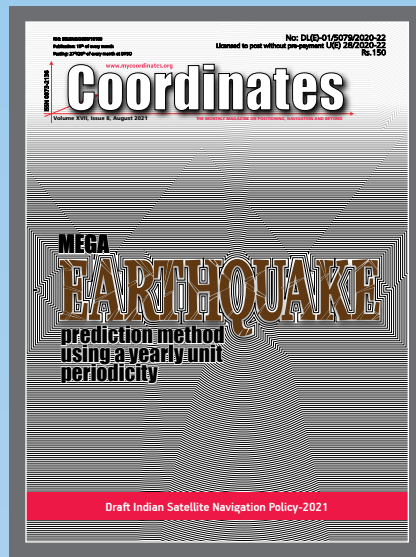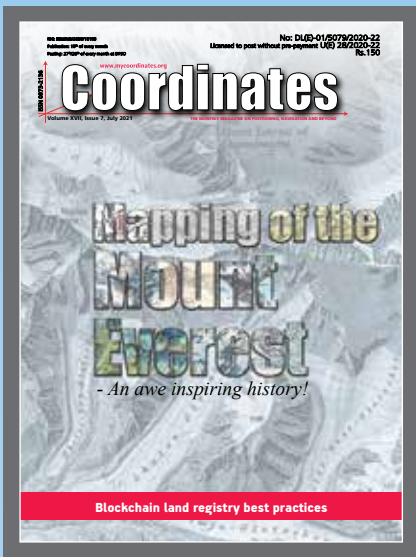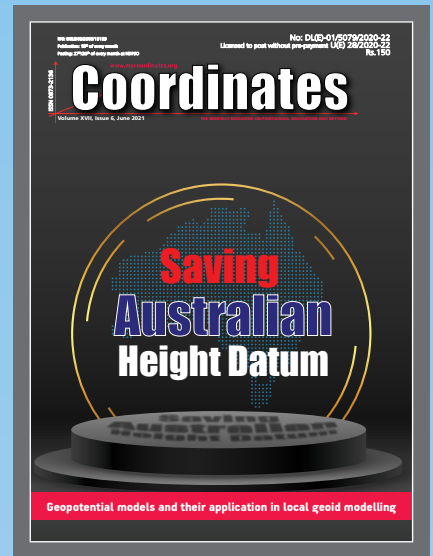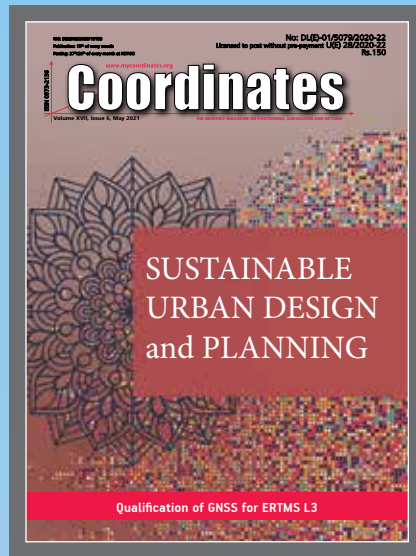
P300 series GNSS tablet

ComNav Technology has released the P300 Series GNSS tablet to the global market. Based on the company's K8 GNSS OEM platform, the high-precision in-cab Android rugged tablet brings innovative performance and ease of use to various operations in precision agriculture, autonomous driving, machine control and other industries. *www.comnavtech.com*

Interface between Vexcel's AMC and IGI's AEROcontrol GNSS/IMU systems introduced

Vexcel Imaging and IGI announced the new interfacing of Vexcel's Adaptive Motion Compensation (AMC) in combination with IGI's industry-leading AEROcontrol GNSS/IMU systems. Both companies worked together to enable the AMC advantage for customers who operate the UltraCam cameras together with IGI's AEROcontrol and CCNS-5.

IGI AEROcontrol is a GNSS/IMU navigation system for the precise determination of the position and altitude of an airborne sensor and/or multiple sensors constellation. This can be the position of the projection center and the angles omega, phi, kappa of an aerial camera and/or any other airborne sensors.

Vexcel's AMC is an innovative motion compensation approach that in addition to correcting image blur in the direction of flight (the so-called Forward Motion Compensation or FMC) also addresses blur caused by multi-directional camera movements during the flight. ◹